Analysis of the field dependence of remanent magnetization curves

R. Egli

Institute of Geophysics, Eidgenossische Technische Hochschule, Zurich, Zurich, Switzerland

Received 12 June 2002; revised 18 October 2002; accepted 30 October 2002; published 7 February 2003.

[1] A new method to calculate and analyze coercivity distributions of measured acquisition/demagnetization curves of remanent magnetization is presented. The acquisition/demagnetization curves are linearized by rescaling both the field and the magnetization axes. An appropriate filtering of the linearized curves efficiently removes measurement errors prior to evaluating the coercivity distributions. The filtered coercivity distributions are modeled using a set of generalized probability density functions in order to estimate the contributions of different magnetic components. An error estimation is calculated for these functions with analytical and numerical methods in order to evaluate whether the model is significantly different from the measured data. Three sediment samples from Baldeggersee (Switzerland) and three samples of urban atmospheric particulate matter (PM) have been analyzed using this method. It is found that the coercivity distributions of some of the magnetic components show significant and consistent deviations from a logarithmic Gaussian function. Large deviations are found also in the coercivity distributions of theoretical AF demagnetization curves of single-domain and multidomain particles. Constraints in the shape of model functions affect the identification and quantification of magnetic components from remanent magnetization curves and should be avoided as far as possible. The generalized probability density function presented in this paper is suitable for appropriate modeling of Gaussian and a large number of non-Gaussian coercivity distributions. *INDEX TERMS:* 1540 Geomagnetism and Paleomagnetism: Rock and mineral magnetism; 1519 Geomagnetism and Paleomagnetism: Magnetic mineralogy and petrology; 1512 Geomagnetism and Paleomagnetism: Environmental magnetism

Citation: Egli, R., Analysis of the field dependence of remanent magnetization curves, *J. Geophys. Res.*, *108*(B2), 2081, doi:10.1029/2002JB002023, 2003.

1. Introduction

[2] Two of the main tasks of environmental magnetism are the identification and the quantification of different magnetic phases in a sample, a procedure usually referred to as the unmixing of magnetic components. Two approaches have been developed for this purpose: multiparameter records [*Thompson*, 1986; *Yu and Oldfield*, 1989; *Verosub and Roberts*, 1995; *Geiss and Banerjee*, 1997] and analysis of magnetization curves [*Thompson*, 1986; *Robertson and France*, 1994; *Carter-Stiglitz et al.*, 2001]. The multiparameter approach is experimentally simple and relies on the measurement of different bulk magnetic properties such as isothermal remanent magnetization (IRM), anhysteretic remanent magnetization (ARM), susceptibility, and hysteresis parameters. Each parameter is a function of the concentration of the various magnetic components. The concentrations can be estimated if the measured parameters are known individually for each component (forward modeling). However, the relation between the physical and chemical properties of the magnetic grains (e.g., composition, grain size, and grain shape) on the one hand and their magnetic properties on the other is complex and usually unknown. Many rock magnetic studies are based on synthetic samples, but the magnetic properties of such samples can differ substantially from their natural counterparts. On the other hand, natural magnetic components can rarely be measured alone, since natural samples often represent complex mixtures of more or less altered magnetic crystals with different origins and histories.

[3] The second approach is based on detailed measurement of induced magnetizations (hysteresis loops) or remanent magnetizations (IRM, ARM, and thermoremanent magnetization (TRM)) in variable magnetizing or demagnetizing fields. The absolute value of the first derivative of these curves is proportional to the contribution of all magnetic grains with a given intrinsic coercivity to the total magnetization of the sample and is called the coercivity distribution. If magnetic interactions between the grains of different components are negligible, the magnetization of a sample is a simple linear combination of the contributions of each magnetic component (finite mixture model with linear additivity). The coercivity distribution of each magnetic component is given by a particular (unknown) function of the magnetizing or demagnetizing field (end-member distribution), and the measured coercivity distribution is a linear combination of these model functions. If all end-

0148-0227/03/2002JB002023$09.00

member distributions are compatible with a parameterized function, such model functions can be used to fit the measured data. If n is the number of components and k the number of parameters of the model function, there are nk parameters which can be adjusted to obtain a model curve that best reproduces the measurements. This operation, called component analysis, is performed with nonlinear fitting algorithms [*Heslop et al.*, 2002]. The coefficient, which multiplies each model function, is a measure of the magnetic contribution of the corresponding component. This approach was first proposed by *Robertson and France* [1994] by assuming that the IRM acquisition curve of each magnetic component can be closely approximated by a cumulative logarithmic Gaussian function with three parameters (amplitude, median destructive field, and dispersion parameter). They also proposed a physical model to explain this assumption. A first application of component analysis with IRM acquisition curves was described by *Eyre* [1996] on Chinese loess samples. The intriguing advantage of this approach is that a detailed knowledge of the magnetic properties of the components is not necessary. The magnetic properties are described by the parameters of the model function used in the component analysis, and the value of these parameters is deduced from the shape of the measured magnetization curve. Furthermore, the same type of magnetization is measured under the same physical conditions for all components, allowing a direct comparison between all magnetic contributions. This approach, however, is limited by its extreme sensitivity to measurement errors and to the shape of the function chosen to model the end-member distributions. *Stockhausen* [1998] handled the effect of measurement noise by introducing goodness-of-fit parameters to indicate how well a measured curve is fitted by a set of model functions. *Kruiver et al.* [2002] proposed a statistical test to compare different models for the component analysis and to decide the number of end-member distributions that are necessary to fit the measured data sufficiently well. They also developed an alternative approach to component analysis, based on a rescaling of the IRM acquisition curve (called linear acquisition plots (LAP)) so that a cumulative Gaussian function is transformed into a straight line (called standardized acquisition plot (SAP)). The SAP of a mixture of slightly overlapped components with logarithmic Gaussian coercivity distributions is characterized by straight segments separated by inflections.

[4] Another important aspect of component analysis is the modeling of end-member coercivity distributions. Previous work has shown that natural and artificial end-member distributions can be approximated with logarithmic Gaussian functions [*Robertson and France*, 1994; *Stockhausen*, 1998; *Kruiver et al.*, 2001]. However, this is not necessarily true for all samples, since many factors, including magnetic interactions, affect the shape of magnetization curves. Theoretical AF demagnetization curves of noninteracting single-domain particles [*Egli and Lowrie*, 2002] and of multidomain particles [*Xu and Dunlop*, 1995] cannot be modeled with logarithmic Gaussian functions. This also applies for experimental AF demagnetization curves of artificial samples of sized magnetite [*Bailey and Dunlop*, 1983; *Halgedahl*, 1998]. In all the cases mentioned above there is only one magnetic component, however, deviations from a logarithmic Gaussian function could be interpreted as the result of the sum of two components with strongly overlapping coercivities. The latter argument is of fundamental importance in the interpretation of component analysis, since it is directly related to the number of inferred components.

[5] We propose here a new approach to the component analysis of acquisition and demagnetization curves. First, we handle the problem of evaluation and removal of measurement noise without the use of component analysis. In this way, filtered coercivity distributions and confidence margins can be calculated without any assumptions about the magnetic composition of the sample. We then handle the problem of component analysis by introducing the use of generalized probability distribution functions (PDFs) to model end-member coercivity distributions without any restrictive assumptions about their shape. We also obtain an error estimation for the distribution parameters used for the component analysis. The latter is of fundamental importance when end-member coercivity distributions of different samples are compared. Finally, this approach is tested on three lake sediment samples.

2. Calculation of Coercivity Distributions

2.1. General Properties of Coercivity Distributions

[6] Coercivity distributions are defined as the absolute value of the first derivative of progressive acquisition or demagnetization curves. We indicate the coercivity distribution with $f_X(H)$, where the index X indicates the original acquisition or demagnetization curve used to calculate f, and H is the magnetic field. Furthermore, $f_X(H)dH$ is the contribution of all coercivities between H and $H + dH$ to the magnetization indicated by X. Magnetic interactions and thermal activation effects produce differences between the different kinds of magnetizations (IRM and ARM) and the different kinds of demagnetizations (DC or AF), so that a rigorous physical interpretation of $f_X(H)$ is almost impossible. However, coercivity distributions can supply a lot of information about the carriers of magnetization and help in the discrimination between different magnetic components. We define here a magnetic component as a set of particles with identical mineralogy and similar physical properties (e.g., grain size and grain shape, morphology, crystallization degree, and concentration of defects): examples are the bacterial magnetosomes [*Moskowitz et al.*, 1988], chemically grown fine magnetite in soils [*Maher and Taylor*, 1988], and detritial magnetite or hematite from a given host rock. The coercivity distribution of a component is characterized by a simple-shaped functions (e.g., a lognormal distribution or a negative exponential distribution), whose shape is controlled by the statistical distribution of the magnetic properties of the particles. Often, coercivity distributions of different components cover the same range of coercivities (e.g., different magnetites) or the contribution of one of them is orders of magnitude weaker with respect to the others (e.g., hematite compared to magnetite). For this reason, the contributions of different components are difficult to recognize directly from the acquisition or demagnetization curves but are evident in the coercivity distributions.

[7] Coercivity distributions are mathematically described by PDFs and can be calculated on different field scales for better isolation of different components. The shape of a

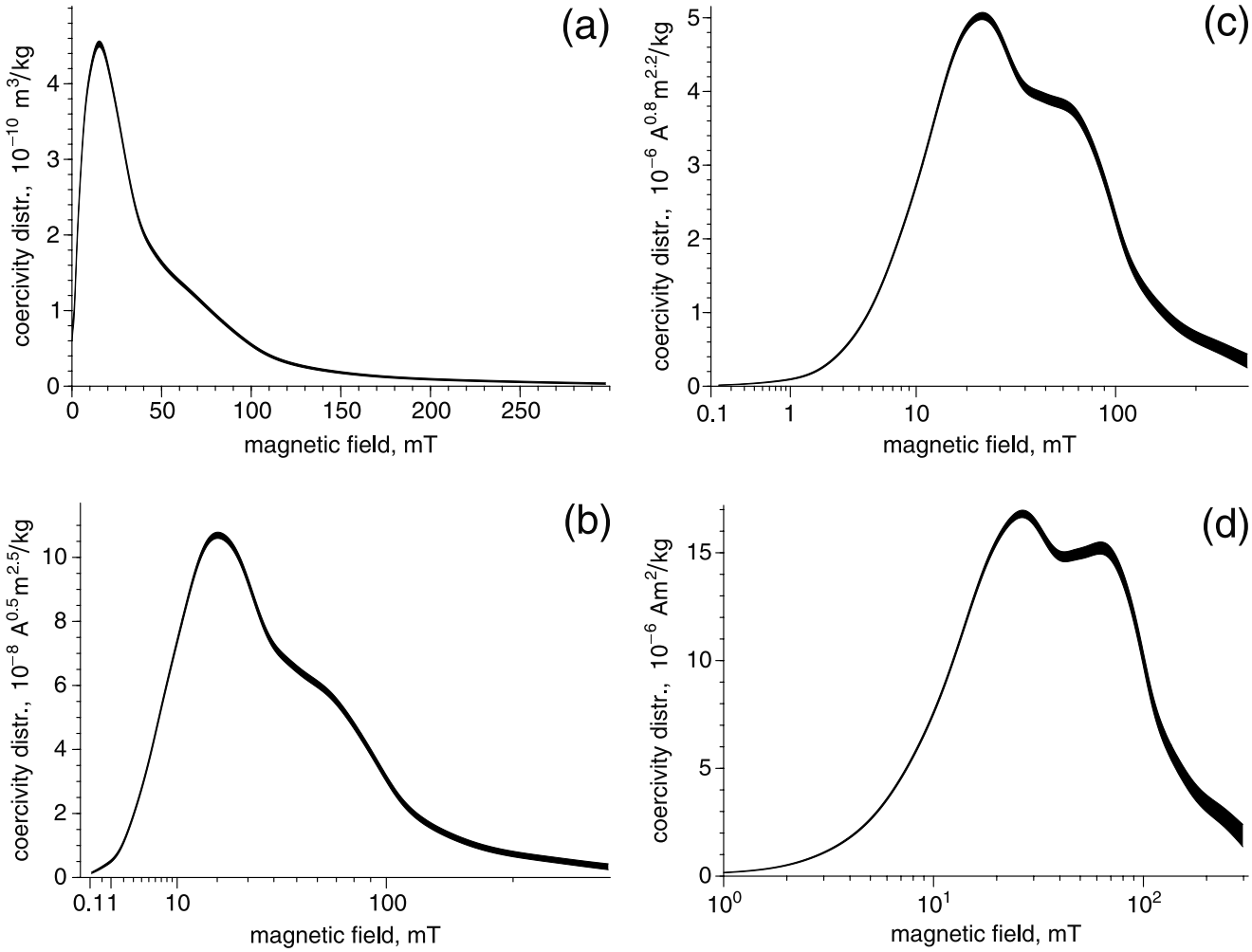

Figure 1. Effect of field rescaling on the shape of a coercivity distribution (sediment sample G010 from Baldeggersee, Switzerland). Four different field scales were chosen: (a) linear field scale, (b) power field scale according to (3) with exponent $p = 0.5$, (c) power field scale according to (3) with exponent $p = 0.2$, and (d) logarithmic field scale. Notice how the second peak of the coercivity distribution increases in amplitude when the field scale approaches a logarithmic scale. The thickness of the curve represents the estimated error of the coercivity distribution. The field scale transformation has an effect also on the absolute error of the coercivity distribution.

coercivity distribution changes according to the field scale adopted, because the integration over all coercivities corresponds to the total magnetization of the sample (normalization property). The scale change of a distribution f generates a new distribution f^* defined by the following transformation rule:

$$H^* = g(H^*); \quad f^*(H^*) = f\left(g^{-1}(H^*)\right)\frac{d}{dH^*}g^{-1}(H^*) \qquad (1)$$

where H^* is the new field scale, g the transformation rule between the old and the new scale, expressed by an injective function with inverse g^{-1}, and f^* the coercivity distribution with respect to the new scale. For example, the transformation rule from a linear to a logarithmic scale is expressed as follows:

$$H^* = \log H; \quad f^*(H^*) = \ln 10 \cdot 10^{H^*} f\left(10^{H^*}\right) \qquad (2)$$

Another useful transformation is the following:

$$H^* = H^p; \quad f^*(H^*) = \frac{(H^*)^{1/p-1}}{p} f\left((H^*)^{1/p}\right) \qquad (3)$$

where p is a positive exponent. We will refer to this transformation as the power transformation. The power transformation converges for $p \to 0$ to the logarithmic transformation. If $0 < p < 1$, high coercivities are quenched on the field scale, and distributions with large coercivities are enhanced. The same effect is obtained with a logarithmic scale and the opposite effect with $p > 1$. The effect of the field scale transformation on the shape of a coercivity distribution is illustrated in Figure 1.

2.2. Calculation of Coercivity Distributions From a Measured Remanence Curve

[8] As pointed out in section 2.1, a coercivity distribution is the absolute value of the first derivative of a stepwise

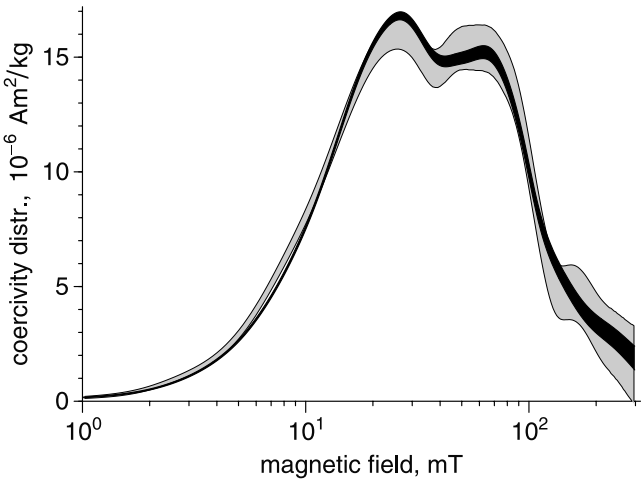

Figure 2. Effect of the measurement precision on the shape and significance of the resulting coercivity distributions. The black line represents the coercivity distribution calculated from the average of eight demagnetization curves of the same sample shown in Figure 1 (G010). The thickness of the line is the estimated error of the distribution. The gray band represents the coercivity distribution calculated form only one demagnetization curve of the same sample; its thickness is the corresponding error estimation. The two distributions are identical within the estimated error, indicating the significance of the error estimation. The presence of two peaks in the coercivity distribution is evident already from the result of a single measurement curve. However, a third peak at 105 mT is not significant and disappears when more precise measurements are done. This demonstrates the importance of an appropriate error estimation for the correct interpretation of coercivity distributions.

acquisition or demagnetization curve. In terms of Fourier analysis, the first derivative is equivalent to a high pass filter, whose effect is to enhance small details of the original curve. For this reason, any information contained in the original curve will be more evident in the resulting coercivity distribution. This applies also to the measurement errors, which are generally small in the measured curve but are enhanced in the resulting derivative. The increase of small measurement errors is the main reason why coercivity distributions have not been used very often in the interpretation of magnetic measurements, despite the potential advantages. Possible sources of measurement errors are discussed in section 2.5. Depending on the curvature of the acquisition/demagnetization curve, a minimum number of steps are required to reproduce the coercivity distribution free from aliasing effects. The amplitude of measurement errors and the number of measured points strongly affect the calculated coercivity distributions, so that changes in the measuring procedure can produce apparently different results. Figure 2 shows the effects of measurement errors on two coercivity distributions of the same sample measured with different degrees of precision.

[9] Measurement errors are commonly removed by fitting the measured acquisition/demagnetization curve with an arbitrary number of given model curves (cumulative logarithmic Gaussian distributions). These model curves are identified with the magnetic signal of individual components. In this way, the calculation of a coercivity distribution rely on its interpretation in terms of component analysis. A way to calculate coercivity distributions without any further interpretation consists in filtering the measurements or the resulting coercivity distributions in order to remove the measurement noise. Often, the measured curves are asymmetric and require a different degree of filtering at different fields. A standard low-pass filter would therefore be inefficient in some regions of the curve, while it would significantly affect the shape of the curve in others.

[10] In the following, we present a technique that permits the removal of the measurement noise homogeneously along the entire curve and simultaneously estimates the error of the resulting coercivity distribution. The latter is particularly useful to avoid misinterpretations of numerical artifacts. The method presented here is based only on the following assumption: all acquisition/demagnetization curves have two regions where the corresponding coercivity distribution is zero on a logarithmic field scale, one at $H \rightarrow 0$ and the other at $H \rightarrow \infty$. In other words, any acquisition/demagnetization curve has two horizontal asymptotes on a logarithmic field scale. The physical meaning of this assumption for $H \rightarrow \infty$ is obvious: all magnetic minerals have a maximum finite coercivity. For $H \rightarrow 0$, the physical explanation is related to thermal activation processes in SD and PSD particles and with domain wall motions in MD particles. Measurements with a sufficient number of points near $H = 0$ are necessary in order to obtain a correct coercivity distribution for small fields. Appropriate scaling of field and magnetization allows linearization of the acquisition/demagnetization curve. On the linearized curve, each measurement point and the related error have the same relative importance, so that a simple low-pass filter can be applied to remove the measurement noise with the same effectiveness for all coercivities. An acquisition/demagnetization curve $M = M(H)$ can be linearized in a simple way by rescaling the field according to the transformation rule $H^* = M(H)$. However, because of the measurement errors, the function $M(H)$ is unknown. A good degree of linearization is reached when a model function $M_0(H)$ expressed by analytical functions is taken as transformation rule instead of $M(H)$. The choice of the appropriate model function $M_0(H)$ becomes simpler if field and magnetization are both rescaled. If $M^* = \mu(M)$ and $H^* = g(H)$ are the rescaling functions for the field and the magnetization, respectively, then the model function is given by $M_0(H) = \mu^{-1}(g(H))$. The relation $M^*(H^*)$ between scaled field and scaled magnetization approaches a straight line when the model function $M_0(H)$ approaches the (unknown) noise-free magnetization curve. The curve defined by $\varepsilon(H^*) = M^*(H^*) - H^*$ represents the deviations of $M^*(H^*)$ from a perfect linear relation. We call $\varepsilon(H^*)$ the residual curve. If the model function $M_0(H)$ used for the scaling procedure is identical with the noise-free magnetization curve, then the residual curve contains only the measurement errors. In reality, since it is impossible to guess the noise-free magnetization curve, the residual curve is a superposition of the nonlinear component of $M^*(H^*)$ and the measurement errors. The fundamental advantage of considering the residual curve instead of the original curve is that the measurement errors

are highly enhanced in the residual curve and can be homogeneously removed with a low-pass filter. The choice of the filter parameters is not critical and has little effect on the shape of the resulting coercivity distribution. Under ideal conditions, $\varepsilon(H^*)$ represents the measurement errors, which can be simply removed by fixing $\varepsilon(H^*) = 0$.

[11] The filtered residual curve can be transformed back into a magnetization curve as follows:

$$M(H) = \mu^{-1}\left[\mathsf{L}\left[\varepsilon\left(g^{-1}(H)\right)\right] + g^{-1}(H)\right] \quad (4)$$

where $\mathsf{L}(.)$ is the low-pass filter operator. $M(H)$ is now supposedly free of measurement errors.

2.3. Coercivity Distribution Calculator (CODICA): A Computer Program for Coercivity Spectra Calculation

[12] CODICA is a computer program based on the scaling method described in section 2.2. It calculates a coercivity distribution from an acquisition/demagnetization curve and gives an estimation of the maximal error of the calculated distribution. The latter is important for evaluating the significance of component analysis on the resulting coercivity distribution. CODICA is available from the author on request.

[13] CODICA runs on a *Mathematica* interface and uses several built-in mathematical routines. The functions of the program are discussed step by step in Appendix B. The results of the main processing steps of a real measurement are shown in Figure 3. The original demagnetization curve is shown in Figure 3a and is characterized by a typical heavy-tailed behavior at high fields. A first scale transformation is applied to the field axis in order to approach a symmetric sigmoidal function (Figure 3b). The second scale transformation is applied to the magnetization axis in order to linearize the demagnetization curve (Figure 3c). Deviations of the linearized demagnetization curve from a best-fit line are plotted in the next step (Figure 3d): the resulting curve corresponds to the residual curve discussed in section 2.2. Further rescaling of the field axis allows to obtain a residual curve that is almost sinusoidal (Figure 3e). Its Fourier spectrum is concentrated in a narrow band around a dominant wavelength, so that a simple low-pass filter easily removes the high-frequency measurement noise with little effect on the final shape of the filtered demagnetization curve. Finally, the filtered residuals (Figure 3f) are converted back to the original demagnetization curve by reversing the previous rescaling steps. The result is a demagnetization curve, which is supposed to be free from measurement errors. A coercivity distribution is obtained from the first derivative of the filtered demagnetization curve (Figure 1). The error estimation is displayed as an error band on the plot (Figure 1) and in a separated plot as a relative error.

2.4. Testing CODICA

[14] CODICA was tested using a synthetic coercivity distribution given by $f(\log H) = N(\log H, 24, 0.36) + 0.04N(\log H, 56, 0.12) + 0.01w(\log H)$, where $N(x, \mu, \sigma)$ is a Gaussian function with median μ in mT and dispersion parameter σ, and $w(x)$ is a Gaussian white noise with variance 1 (Figure 4). This coercivity distribution is the sum of two components with overlapping coercivities and different concentrations, which are similar to those encountered in the natural samples presented later in this paper. The efficiency of CODICA in removing the measurement errors is compared with a common low-pass filter. Different cutoff frequencies were chosen, and the mean square difference between the filtered and the noise-free distributions was calculated. The results are given in Figure 5a. Because the distorting effects introduced by a low-pass filter are mostly avoided after rescaling the magnetization curve, better results are obtained with CODICA. The distorting effects introduced by the application of low-pass filters were further tested by comparing the component analysis of the noise-free and the filtered coercivity distributions. Changes in the shape of the coercivity distribution are related to changes in the fitting parameters. The difference between the original parameters of the synthetic coercivity distribution and the best-fit parameters of the filtered distributions are plotted in Figure 5b. Optimum removal of the measurement noise can be obtained without significant changes of the fitting parameters. Consequently, the results of a component analysis are not affected by the filtering procedure of CODICA.

2.5. Measurement Errors

[15] Measurement errors are the main limiting factor in the interpretation of finite mixture models. Some knowledge about the measurement errors is useful to evaluate the significance of a component analysis and to optimize the measurement procedure. Measurement errors may arise from (1) errors in the magnetization measurement, (2) errors in the application of the magnetization/demagnetization field, (3) errors induced by viscosity effects if the time interval between the application of the field and the measurement is not the same for all steps, and (4) errors induced by mechanical unblocking of magnetic particles under application of high magnetic fields on unconsolidated samples. These error sources generate different noise signals that affect the measurement. Simple error propagation equations can be used to estimate the amplitude of the errors; some results are listed in Appendix A. The effect of the four measurement error sources on the calculation of a coercivity distribution is simulated graphically in Figure 6. Mechanical unblocking effects can account for large errors at high fields, which are occasionally observed in some unconsolidated samples obtained by pressing a powder in plastic boxes. Magnetic grains that are electrostatically attached to larger clay particles are good candidates for such undesired effects. Mixing the sample powder with nonmagnetic wax before pressing it has been found to be a good solution to reduce measurement problems at high fields (S. Spassov, personal communication).

3. Component Analysis With Coercivity Distributions

[16] In section 2, we have shown how measurement noise in acquisition/demagnetization curves can be filtered so that errors affecting the calculation of coercivity distributions are minimized. Now we turn to the problem of component analysis.

3.1. The Finite Mixture Model

[17] Consider a sample which contains a mixture of n different magnetic components (finite mixture model). Each component has a probability distribution $f_i(H|\theta_i)$ for the intrinsic coercivity, which depends on a set of distribution

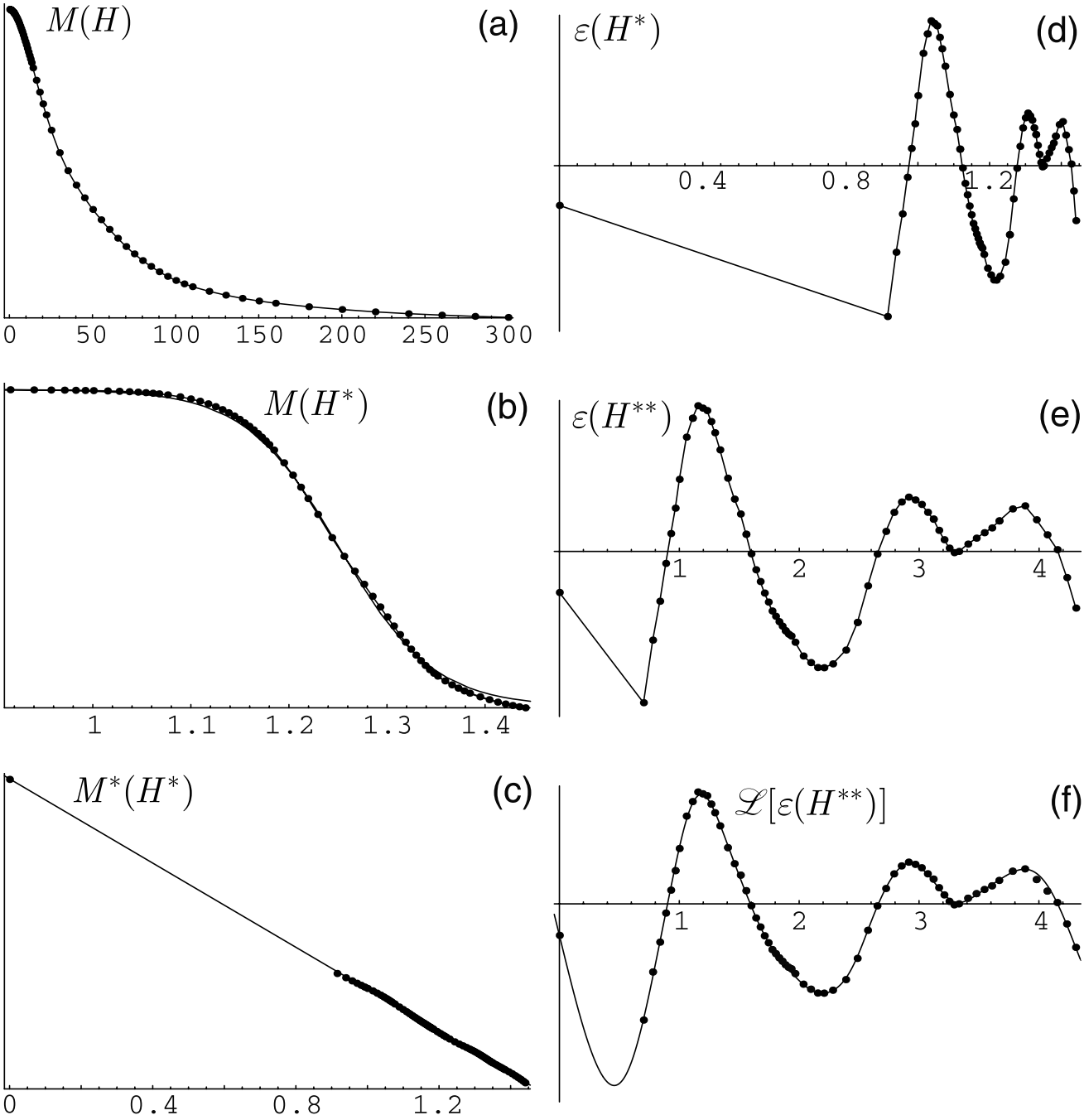

Figure 3. Calculation of a coercivity distribution using CODICA. Each plot is the original output of a program step, as discussed in the text. (a) Original data for the AF demagnetization of an ARM (sample G010, as in Figures 1 and 2). (b) Demagnetization curve with rescaled field compared with a best-fitting tanh function (solid line). The scaling exponent was $p = 0.064$. (c) Demagnetization curve with rescaled magnetization and best-fitting line. (d) Residual curve. (e) The residual curve in (d) was rescaled in order to approach a sinusoidal curve. (f) A low-pass filter was applied to the residual curve in order to remove the measurement errors. A back-transformation of the filtered residuals through the steps shown in (d), (c), and (b) and subsequent numerical derivation gives the coercivity distribution plotted in Figure 1.

parameters $\boldsymbol{\theta}_i = (\theta_{i1}, \ldots, \theta_{il})$. If the magnetization of each component adds linearly to the others (linear additivity), the bulk coercivity distribution of the sample is given by:

$$f(H) = \sum_{i=1}^{n} c_i M_{ri} f_i(H|\boldsymbol{\theta}_i) \tag{5}$$

where c_i and M_{ri} are the concentration and the saturated magnetization of the ith component, respectively. The bulk magnetization is given by the sum of the magnetizations of each component. Generally, $f_i(H|\boldsymbol{\theta}_i)$ is modeled with a logarithmic Gaussian function [*Robertson and France*, 1994].

[18] In case of interactions, linear additivity no longer holds. The shape of $f(H)$ depends on the magnetization process and may differ for acquisition and demagnetization curves [*Cisowski*, 1981]. Linear additivity is destroyed by interaction effects which may easily occur in synthetic mixtures [*Lees*, 1997]. *Carter-Stiglitz et al.* [2001] avoided this problem in their synthetic samples by dispersing potentially interacting pure components in a diamagnetic matrix before mixing them. Their dispersed pure samples were taken as end-member components for their unmixing tests. A particular case is given in samples where each magnetic component is formed by clusters of similar particles. Consequently, strong interactions exist within but not between the clusters, provided the volume concentration of the clusters is low enough. In this case, (5) can be rewritten to:

$$f_{\text{int}}(H) = \sum_{i=1}^{n} c_i M_{ri}(C_i) f_i^*(H|\boldsymbol{\theta}_i, C_i) \tag{6}$$

where C_i is the volume concentration of the grains of the ith component within the clusters. Linear additivity is preserved in this case. Equation (6) may apply for the synthetic samples of *Carter-Stiglitz et al.* [2001] and in natural samples.

3.2. Generalized Coercivity Distributions

[19] Except for artificial samples, the end-member coercivity distributions of a mineral mixture are unknown, and model functions $f(x|\boldsymbol{\theta})$ with a set $\boldsymbol{\theta}$ of parameters are used instead. A lognormal function is commonly assumed for $f(x|\boldsymbol{\theta})$. In this case $\boldsymbol{\theta} = (H_{1/2}, DP)$, where $H_{1/2}$ is the median destructive field and DP the dispersion parameter [*Robertson and France*, 1994; *Kruiver et al.*, 2001; *Heslop et al.*, 2002]. On a logarithmic field scale, the lognormal function coincide with the Gauss distribution. Accordingly, an end-member distribution is forced to be symmetrical about log $H_{1/2}$ and to have a fixed "curvature." Skewed, more "squared" or less "squared" distributions cannot be represented in this way. Deviations of $f(x|\boldsymbol{\theta})$ from a logarithmic Gaussian function are possible, since the relation between chemical and geometric properties of the grains on the one hand and magnetic properties on the other are rather complex and nonlinear. In this paper, we will demonstrate the existence of consistent and systematic deviations from the logarithmic Gaussian distribution model in some natural and artificial samples. These deviations can significantly affect the results of unmixing models.

[20] As shown in section 3.1, an end-member coercivity distribution is conveniently described by a PDF called $f(x)$ in the following. The shape of $f(x)$ is controlled by a set of distribution centers μ_n with related dispersion parameters σ_n, with $n \in \mathbb{N}$ [*Tarantola*, 1987]. Special cases are given when $n = 1$ (μ_1 is the median, σ_1 the mean deviation), $n = 2$ (μ_2 is the mean, σ_2 the standard deviation), and $n \to \infty$ (μ_∞ is the midrange and σ_∞ the half-range). The parameters $H_{1/2}$ and DP used by *Robertson and France* [1993] correspond to μ_2 and σ_2 on a logarithmic field scale. The symmetry of a PDF is described by the coefficient of skewness s, where $s = \sigma_3^3/\sigma_2^3$ [*Evans et al.*, 2000]. Symmetric distributions are characterized by $s = 0$ and $\mu_n = \mu_2$. The curvature of a PDF is described by the coefficient of excess kurtosis k, where $k = \sigma_4^4/\sigma_2^4 - 3$ [*Evans et al.*, 2000]. The Gaussian PDF is characterized by $k = 0$.

[21] The description of small deviations from a Gaussian PDF involves the use of functions with more than two independent parameters. It is of great advantage if such functions maintain the general properties of a Gauss PDF: the nth derivative should exist over $\mathbb{R}$ and $\sigma_n < \infty$ for all values of $n \in \mathbb{N}$. Furthermore, the Gaussian PDF should be a particular case of such functions. A good candidate is the generalized Gaussian distribution *GG* [*Tarantola*, 1987], known also as the general error distribution [*Evans et al.*, 2000]. The Gaussian PDF is a special case of *GG* distributions. Other special cases are the Laplace distribution and the box distribution. The *GG* distribution is symmetric: $s = 0$.

[22] Skewed distributions can be obtained from a symmetric PDF through an appropriate variable substitution $x^* = g(x,q)$, where q is a parameter related to the skewness and $g(x,q_0) \equiv x$ for a given value q_0 of q. If these conditions are met, the variable substitution generates a set of distributions with parameter q, wherein the original PDF is a special case. A suitable transformation applied to the *GG* distribution gives the following function:

$$SGG(x,\mu,\sigma,q,p) = \frac{1}{2^{1+1/p}\sigma\Gamma(1+1/p)} \frac{\left|qe^{qx^*} + q^{-1}e^{x^*/q}\right|}{e^{qx^*} + e^{x^*/q}} \cdot \exp\left[-\frac{1}{2}\left|\ln\left(\frac{e^{qx^*} + e^{x^*/q}}{2}\right)\right|^p\right] \tag{7}$$

with $x^* = (x - \mu)/\sigma$ and $0 < |q| \leq 1$. We will call this PDF the Skewed Generalized Gauss Distribution (*SGG*). The *GG* distribution is a special case of (7) for $q = 1$, and the Gauss distribution is a special case of (7) for $q = 1$ and $p = 2$. Approximate relations between the distribution parameters and μ_2, σ_2, s and k for $p \to 2$, $q \to 1$ are listed in Appendix A. Some examples of *SGG* distributions are shown in Figure 7. The four parameters of a *SGG* distribution have a hierarchic structure: μ and σ control the most evident properties of the PDF, namely the position along the x axis and the "width." On the other hand, q and p influence the symmetry and the curvature of the PDF.

[23] The need of generalized distribution functions to model the coercivity distribution of a magnetic component is evident on the examples shown in Figures 8 and 9. Figure 8a shows the theoretical AF demagnetization curve of an ARM for an assemblage of noninteracting, uniaxial single-domain magnetite particles with lognormally distributed volumes and microcoercivities [*Egli and Lowrie*, 2002]. Figure 8c shows the theoretical AF demagnetization curve of an ARM for multidomain particles with a Gaussian distribution of microcoercivities [*Xu and Dunlop*, 1995]. Both cases can be regarded as a single magnetic component. The related coercivity distributions are not Gaussian on a logarithmic field scale but can be fitted well with a *SGG* distribution. Similar coercivity distributions are also found in natural sediments, as the ODP sample of Figures 8e and 8f. The magnetic materials presented in Figure 8 are very different; nevertheless, they have similar coercivity distributions with a negative skewness of -1.3 to -1.7. Similar results are obtained also from AF demagnetization curves of SIRM. Both the magnetic interactions and the magnetic viscosity generally increase the initial slope of an AF demagnetization curve, because they affect mainly low coercivity contributions to the total magnetization. As a

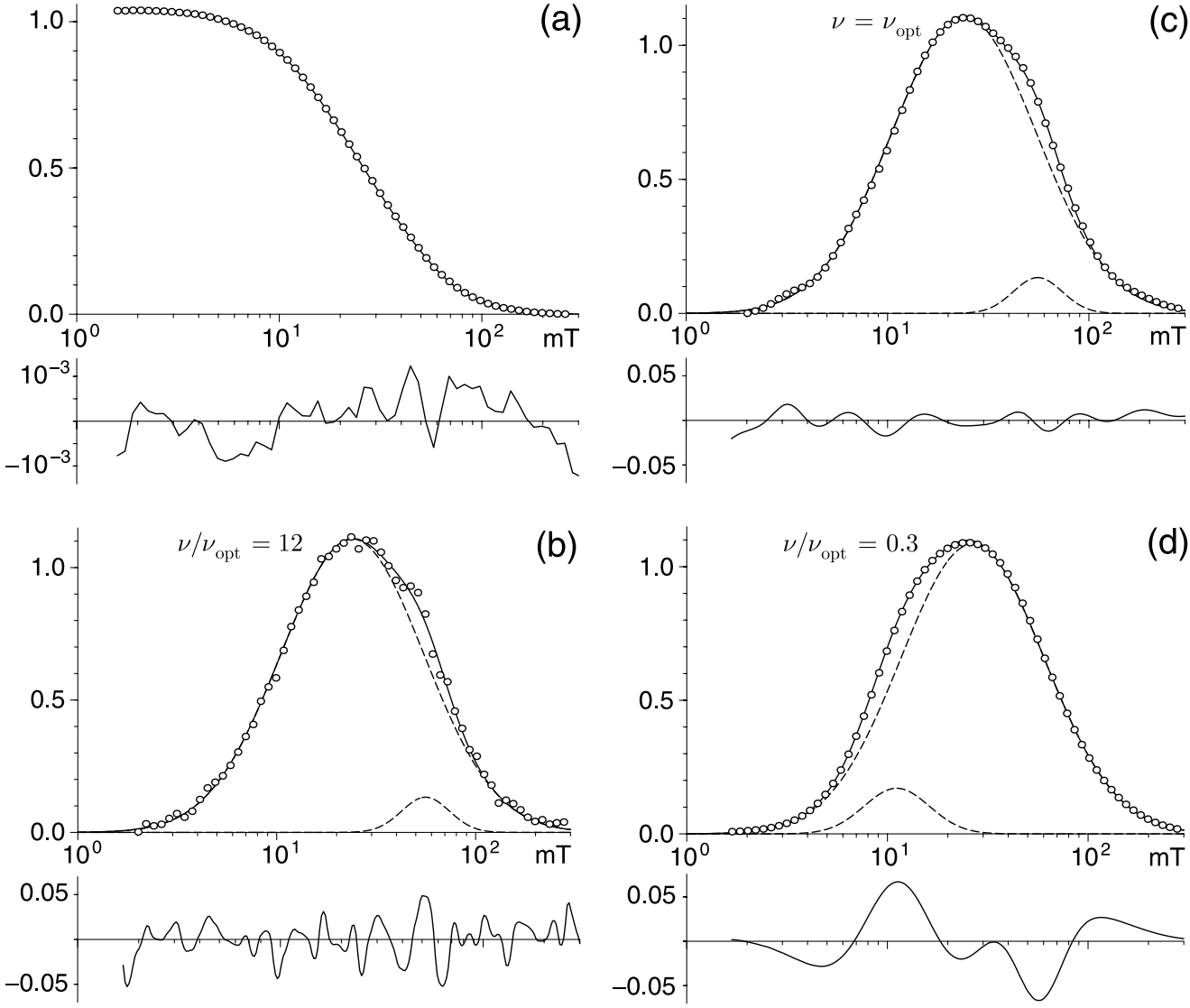

Figure 4. A synthetic example of measurement noise removal with the procedure described in the text. A synthetic coercivity distribution was generated according to the text. The coercivity distribution is the sum of two components with overlapping coercivities and different concentrations. The demagnetization curve in (a) was calculated by numerical integration of $f(\log H)$. This curve was then rescaled according to the procedure described in the text and subsequently low-pass filtered with different cutoff frequencies. The corresponding coercivity distributions (open circles) in (b), (c), and (d) are the numerical differentiation of the filtered curves. A component analysis has been performed on these coercivity distributions. The single components are dashed. At the bottom of each plot, the difference between the original noise-free coercivity distribution and the coercivity distribution calculated from the filtered curves is presented as well. In (b), the cutoff frequency ν was too large and the measurement errors have not been removed. In (d), the cutoff frequency was too small: the measurement errors have been removed completely, but the shape of the coercivity distribution is altered. In (c), the cutoff frequency ν_{opt} was sufficient to remove the measurement errors without a significant alteration of the coercivity distribution. The difference between noise-free and calculated coercivity distribution is minimal, and the result of component analysis is unaffected.

consequence, the related coercivity distributions are left-skewed, and the crossing point between normalized acquisition and demagnetization curves is <0.5 [*Cisowski*, 1981]. However, magnetic interactions and magnetic viscosity can be excluded in the model demagnetization curves of Figures 8a and 8c. In this case, the skewness of the related coercivity distributions is controlled by intrinsic properties of the magnetic grains. In single-domain grains, thermal activation effects produce an asymmetrical shift of the coercivity distribution toward lower fields [*Egli and Lowrie*, 2002], so that a symmetrical distribution of microcoercivities ($s = 0$) generates a left-skewed coercivity distribution ($s < 0$). In multidomain grains, the negative exponential distribution (Figure 7b) plays a critical rule.

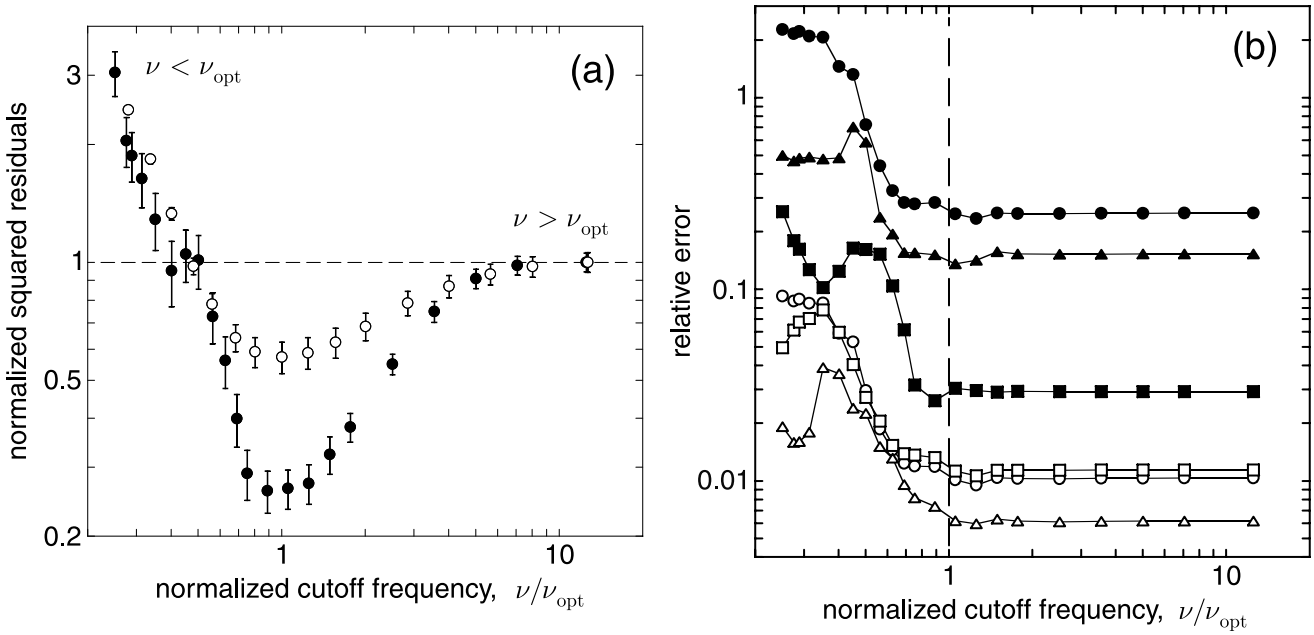

Figure 5. Comparison between measurement noise removal with and without the rescaling procedure described in the text. The same coercivity distribution of Figure 4 was calculated and the operation was repeated 1000 times with different simulations of the measurement error $w(\log H)$. Each of the 1000 distributions was filtered in the same way as in Figure 4. In (a), the mean squared difference between the filtered and the noise-free distributions has been plotted as a function of the normalized cutoff frequency ν of the low-pass filter. Filled symbols refer to the output of CODICA, open symbols to the results obtained by filtering the data without the rescaling procedure of CODICA. The normalizing factor for the cutoff frequency is chosen to be identical with the value of the cutoff frequency, which minimizes the squared residuals. The noise removal is more efficient after the rescaling procedure. In (b), the relative error of the best-fit parameters m, μ, and σ of the two Gaussian distributions are plotted as a function of the normalized cutoff frequency of the low-pass filter. For $\nu < 0.7\nu_{opt}$, a low-pass filter induces significant distortions in the shape of the coercivity distribution. Open symbols refer to the best-fit parameters of the component defined by $m = 0.04$, $\mu = 56$ mT, and $\sigma = 0.12$. Solid symbols to the other component. Circles refer to m, squares to μ, and triangles to σ.

Bailey and Dunlop [1983] have shown that magnetic grains with a multidomain-type result of the modified Lowrie–Fuller test [*Johnson et al.*, 1975] have a microcoercivity distribution which is more convex than the negative exponential distribution. These coercivity distributions are characterized by $s < -1$. Left-skewed coercivity distributions are also needed to fit AF demagnetization curves of a SIRM in artificial samples of sized magnetite with grain sizes between 0.1 and 100 μm [*Bailey and Dunlop*, 1983; *Halgedahl*, 1998], as shown in Figure 9. The coercivity distributions of all grain sizes have a skewness of $s = -0.93 \pm 0.1$, which is close to that of a negative exponential distribution ($s = -0.997$). However, the importance of magnetic interactions in these samples is not clear.

3.3. Error Estimation

[24] Component analysis can be extremely sensitive to measurement errors, especially in case of magnetic components with highly overlapped coercivity distributions. Thus, some distribution parameter estimates may not be significant at all, even if the quality of the measurement is excellent for the usual standards in rock magnetism. An error estimation of each distribution parameter is important to avoid misinterpretations. This problem was first recognized by *Stockhausen* [1998]: he attempted to evaluate the significance of his results by introducing parameters that indicate how well a measured curve is fitted by a set model functions. *Kruiver et al*. [2002] proposed a statistical test to compare different models for the component analysis. However, these approaches are useful to evaluate the overall significance of component analysis (see section 3.4) but do not provide any information about the single components. The latter is obtained with an error estimation for each distribution parameter. Error estimates for each parameter are provided in the following for a general PDF $f(x|\boldsymbol{\theta})$.

[25] We assume the measured distribution to be given by $y_i = f(x_i) + \delta y_i$, where (x_i, y_i) is a measurement point and δy_i the related measurement error. Several methods can be used to obtain an unbiased estimation $\hat{\boldsymbol{\theta}}$ of $\boldsymbol{\theta}$ [*Stockhausen*, 1998; *Kruiver et al.*, 2001; *Heslop et al.*, 2002]. A best-case error estimate is obtained by means of the Rao-Cramér-Frechet inequality (RCF). If $f(x|\theta)$ is a Gauss distribution with variance σ^2, measured at regular intervals Δx of x, and if $\delta y_i = \delta y$ is independent of x_i, the variance of one unknown distribution parameter θ is given by:

$$\mathrm{var}\left(\hat{\theta}\right) \geq \frac{2\pi^{1/2}\sigma\Delta x(\delta y)^2}{\int_X \frac{[\partial_\theta f(x|\theta)]^2}{f(x|\theta)}\,\mathrm{d}x} \tag{8}$$

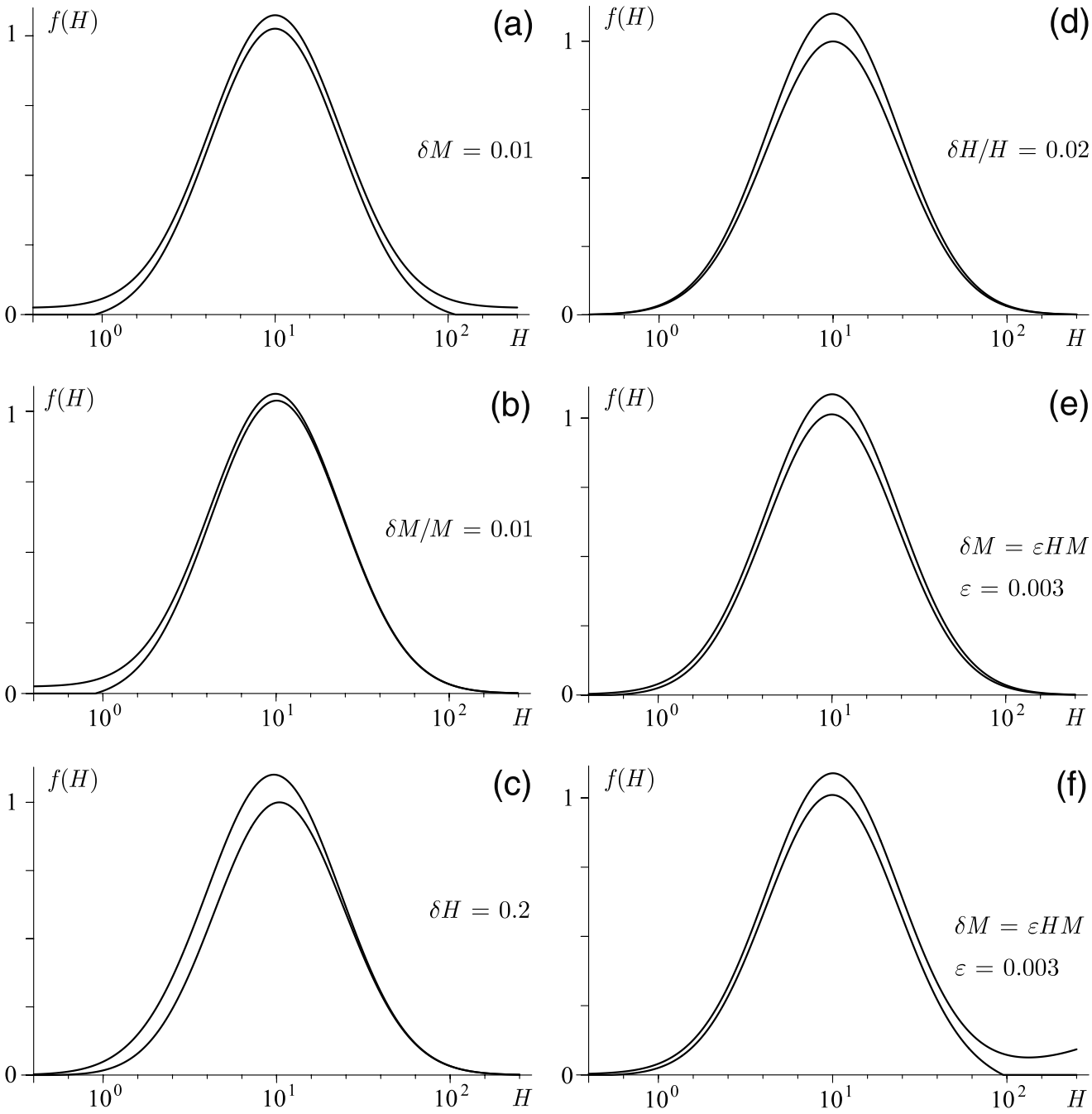

Figure 6. Simulated effect of some measurement error sources on the calculation of a coercivity distribution with following parameters: $m = 1$, $\mu = 10$ mT, and $\sigma = 0.38$ according to the calculations of Appendix A. The two curves of each plot give the upper and lower limit of a coercivity distribution calculated from a demagnetization curve measured at fixed field intervals of 0.2 on a logarithmic field scale ($\Delta H/H \approx 0.585$). Measurements are performed with (a) an absolute measurement error $\delta M = 0.01$, (b) a relative measurement error $\delta M/M = 0.01$, (c) an absolute error of 0.2 mT affecting the applied peak field, and (d) a relative error of 2% affecting the applied peak field. In (e) and (f), measurement errors arise from mechanical unblocking of a part $\varepsilon = 0.3\%$ of all magnetic particles in an unconsolidated sample. In (f), a magnetically harder component (e.g., hematite) with an unremovable magnetization of 5% is added to the soft component.

A proof of equation (8) starting from the standard formulation of the RCF inequality is given in Appendix C. Equation (8) can be used to estimate the minimum errors of the parameter estimates of a *SGG* distribution with $p \to 2$ and $q \to 1$. The results are listed in Appendix A. More precise analytical error estimations, which apply asymptotically to all unbiased parameter estimates, are obtained with error propagation methods, however, only in the limiting

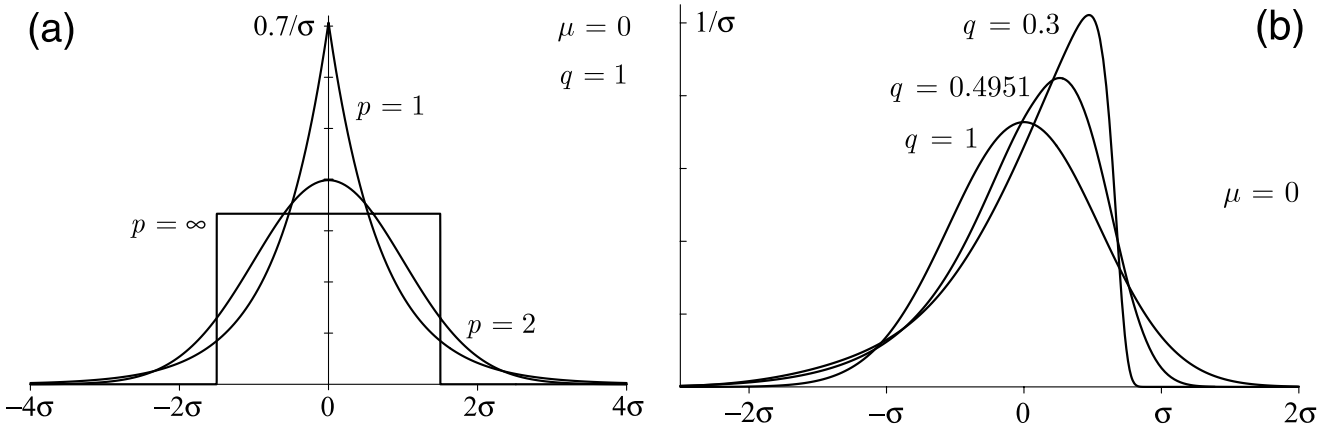

Figure 7. Examples of *SGG* distributions, given by $f(x) = SGG$ (x, μ, σ, q, and p). (a) Some particular cases with, $\mu_2 = 0$, $\sigma_2 = 1$, and $q = 1$ are plotted. The skewness of all curves is zero. Furthermore, $p = 1$ for a Laplace distribution, $p = 2$ for a Gauss distribution, and $p \rightarrow \infty$ defines a box distribution. (b) Some left-skewed SGG distributions with $\mu_2 = 0$ and $\sigma_2 = 0.5484$ are plotted. Right-skewed distributions with the same shape can be obtained by changing the sign of μ and q. Demagnetization curves of multidomain magnetite can be modeled with exponential functions. The corresponding coercivity distribution on a logarithmic field scale can be approximated by a *SGG* distribution with $\sigma = 0.6656$, $q = 0.4951$, and $p = 2.3273$, plotted in (b). The difference between an exponential PDF and its approximation by a *SGG* distribution is smaller than the thickness of the curves.

case of one component. Then, the variance of an unknown distribution parameter θ is given by:

$$\text{var}\,\theta = \frac{\Delta x(\delta y)^2}{\int_X [\partial_\theta f(x|\theta)]^2 \mathrm{d}x} \tag{9}$$

A proof of equation (9) is given in Appendix C. Errors of the unbiased parameter estimates for one *SGG* distribution are listed in Appendix A.

3.4. Significance Tests

[26] The finite mixture model of equation (6) has $n(l + 1)$ independent parameters. If a smaller number of parameters is assumed, the mixture model will not fit well the measured data. There are two possibilities for increasing the number of model parameters. The first one consists of adding more components to the model, as discussed in the literature [*Robertson and France*, 1994: 2 components; *Eyre*, 1996: 4 components; *Stockhausen*, 1998: 2 components; *Kruiver et al.*, 2001: up to 3 components; *Heslop et al.*, 2002: up to 4 components]. The second possibility is presented in this paper and consists of a better definition of the end-member PDF. Both strategies can suggest wrong conclusions, as discussed in section 4, if the unmixing results are not evaluated critically. The problem of finite mixing models is related to the fundamental question of how many parameters should be used to fit experimental data. The addition of new parameters always improves the goodness of fit of a mixture model; however, this improvement is not necessarily significant. *Kruiver et al.* [2001] proposed a combination of statistical tests to determine whether the addition of extra parameters significantly improves the goodness of fit. They apply an F test and a t test to the squared residuals of one fit model with respect to another model to decide if the two models are significantly different. We propose here the use of a Pearson's χ^2 goodness of fit test [*Cowan*, 1998], which allows us to test if an experimental probability distribution is compatible with a given model distribution $f(x|\boldsymbol{\theta})$ with l unknown parameters $\theta_1 \ldots \theta_l$. According to this test, the two distributions are incompatible at a confidence level α (generally $\alpha = 0.05$) if $\chi^2(\boldsymbol{\theta}) > \chi^2_{n-l-1;1-\alpha}$, where $\chi^2_{n-l-1;1-\alpha}$ is the value of the χ^2 distribution with $n - l - 1$ degrees of freedom, evaluated at $1 - \alpha$. A coercivity distribution calculated with the method presented in section 2 can be used as reference distribution for the Pearson's χ^2 goodness of fit test, since this method is not based on finite mixture models.

[27] A statistical test alone is not sufficient to evaluate the significance of a mixing model, as demonstrated in section 4. Sometimes, the coercivity distributions of two magnetic components are widely overlapped, and an extremely high measurement precision is required in order to identify these components. A stack of six demagnetization curves with 72 steps each has been used for the analysis of some samples presented in this paper. Such a high measurement precision cannot be used as a standard for systematic investigations. Nevertheless, an integrated approach to this problem is possible, as shown in section 4 on the example of urban atmospheric particulate samples. In this case, the component analysis of an individual sample was very critical. The accurate choice of three samples with extremely different degrees of pollution allowed to define the number of magnetic components and their magnetic properties. Much less precision would be required for an extended study of urban atmospheric particles. The component analysis of "standard quality" measurements would be supported by the detailed information acquired with the accurate analysis of few reference samples. A similar strategy has been applied to the measurement of the lake sediments presented in section 4. In this case, different sources of magnetic minerals in the sediments were investigated by accurate measurements of each sedimentary unit and of samples

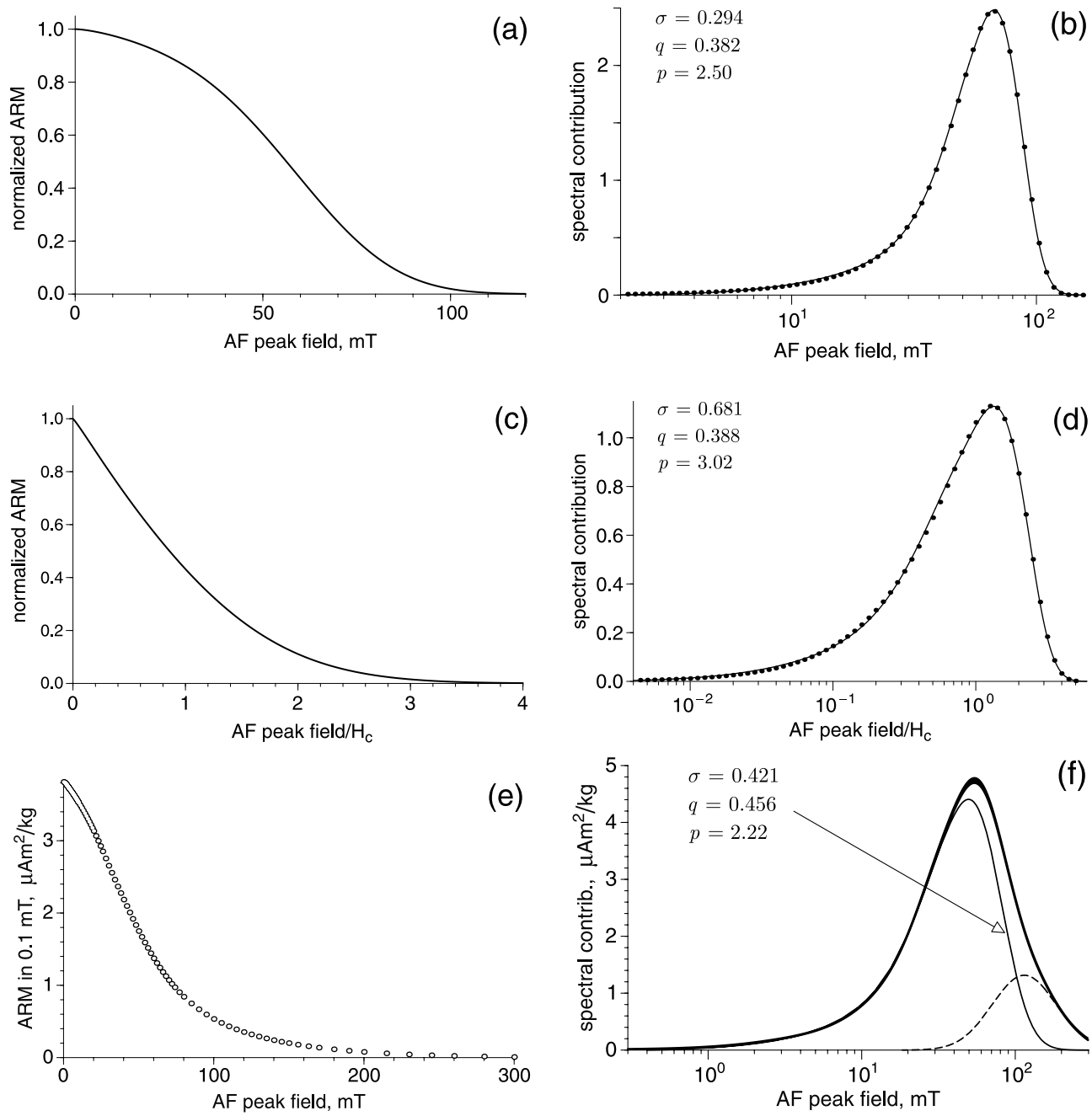

Figure 8. Examples of significant deviations of calculated and measured coercivity distributions from a logarithmic Gaussian function. (a) Theoretical AF demagnetization curve of an ARM imparted to a set of random oriented, noninteracting single domain magnetite particles [*Egli and Lowrie*, 2002]. The particles have lognormally distributed volumes and microcoercivities. The corresponding coercivity distribution (b) is plotted with points and the solid line is the best-fitting SGG function. (c) Theoretical AF demagnetization curve of an ARM imparted to a set of multidomain particles with Gaussian distributed microcoercivities (redrawn from the study of *Xu and Dunlop* [1995]). The corresponding coercivity distribution (d) is plotted with points and the solid line is the best-fitting SGG function. (e) AF demagnetization curve of an ARM imparted to an ODP sediment sample (leg 145) taken in the North Pacific (courtesy of M. Fuller). The corresponding coercivity distribution is shown in (f) together with a component analysis performed with SGG functions. The coercivity distribution of the soft component (solid line) clearly differs from a log-Gaussian function.

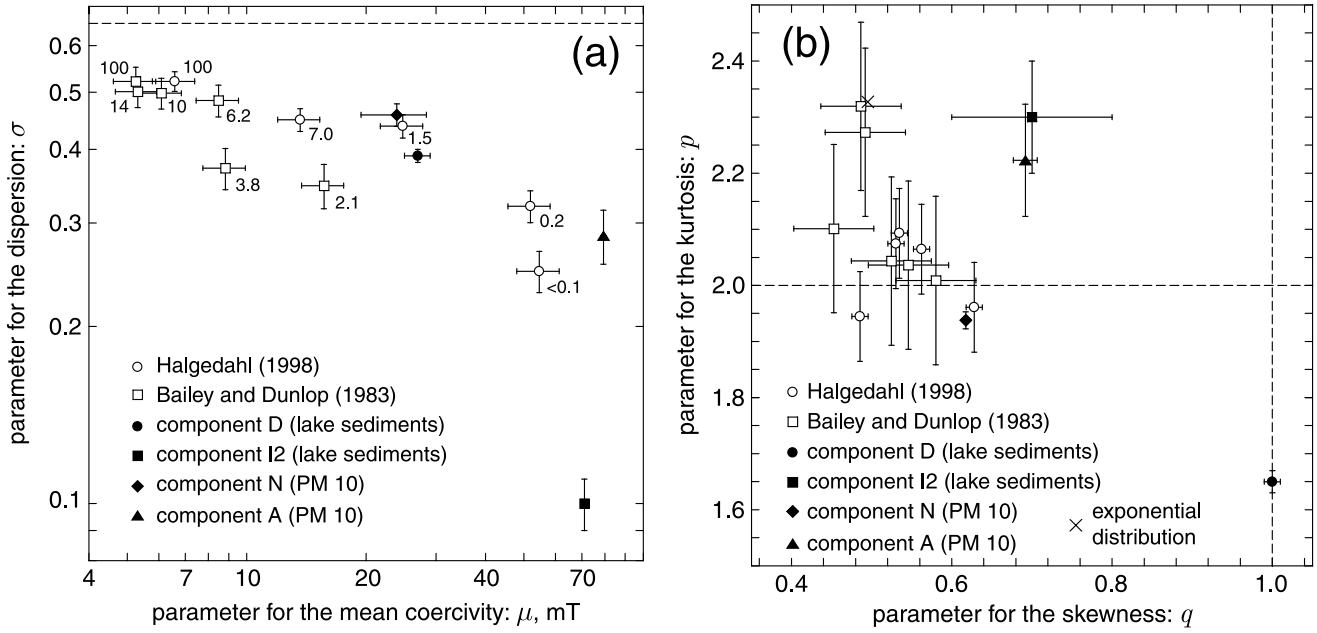

Figure 9. Coercivity distribution parameters μ, σ, q, and p (see text) for the AF demagnetization of IRM in various synthetic samples of sized magnetite. The magnetic components identified in lake sediments and PM10 dust samples are also shown for comparison. Numbers beside each point indicate the grain size in μm. (a) Scatterplot of μ and σ, which are a measure of the median and the width of a coercivity distribution, respectively. The dashed line indicates the value of σ for a negative exponential distribution (Figure 7). Large grains are characterized by low values of μ and high values of σ. Notice the extremely low value of σ measured for component I2 (probably biogenic magnetite). An inverse correlation between μ and σ is evident. (b) Scatterplot of q and p, which are related to the skewness and the kurtosis of a coercivity distribution, respectively. The cross point of the dashed lines corresponds to the values of q and p for a log-Gaussian distribution. All samples of sized magnetite show values of q that are significantly different from those of a log-Gaussian distribution. They group around mean values of $q \approx 0.46$. All parameters of the sized magnetites are intermediate between those of a log-Gaussian distribution and those of a negative exponential distribution. The coercivity distribution of larger grain sizes approaches an exponential distribution.

from the catchment area. Then, AF demagnetization curves with 20 steps were measured for the entire sediment column. The measurements were fitted with the coercivity distributions of the magnetic components identified in three reference samples. Changes in the amount of biogenic magnetite during the last 120 years could be reconstructed in this way.

[28] We propose the following set of conditions to apply and test mixing models to a large set of samples:

1. *Choice of reference samples.* Reference samples containing the most varied amounts of the same set of magnetic components should be chosen for detailed and precise measurements. These samples should define the most extreme conditions to be taken into account by the mixing model.

2. *Statistical tests.* The mixing model has to pass a statistical significance test (goodness of fit test) for each reference sample; in other words it should be compatible with the measured data within the experimental errors.

3. *Errors.* All model parameters should be significant, i.e., they should not be affected by large errors.

4. *Consistency.* The coercivity distributions of the same components should be identical within the experimental error, or they alternatively should show variations which are consistent with some physical or chemical changes. Furthermore, variations in the concentration of each magnetic component should be explained with the help of some independent information (geological setting, chemical and physical processes).

[29] Point 4 implies some knowledge about the potential sources of magnetic minerals (e.g., magnetite formation in soils [*Maher*, 1988], titanomagnetites in volcanic rocks [*Worm and Jackson*, 1999], biogenic magnetite [*Moskowitz et al.*, 1993], and maghemite in loess [*Eyre*, 1996]) and about the properties of magnetization and demagnetization curves [*Dunlop*, 1981, 1986; *Bailey and Dunlop*, 1983; *Johnson et al.*, 1975; *Halgedahl*, 1998; Cisowski, 1980; *Hartstra*, 1982; *Robertson and France*, 1994].

4. Interpretation of Coercivity Distributions by Component Analysis

4.1. Comparison Between Different PDFs

[30] As discussed above, the results of a component analysis depend upon the PDF chosen to model the end-member coercivity distributions and particularly on the number of parameters assigned to each PDF. In this section, we will compare results obtained with a linear combination

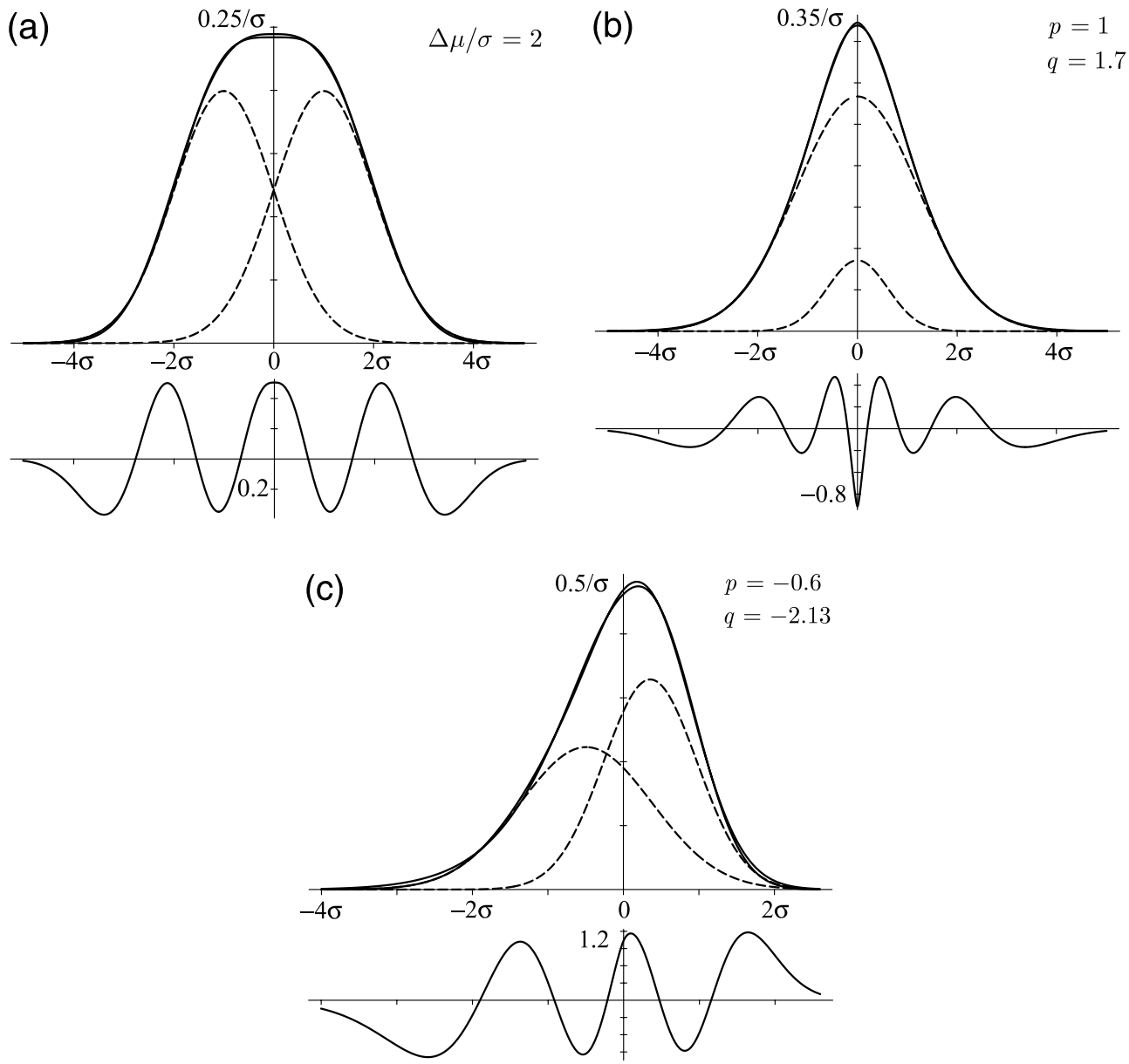

Figure 10. Three cases where a linear combination of two Gaussian functions is very similar to a *SGG* distribution. (a) $mN(x, \mu_1, \sigma) + mN(x, \mu_2, \sigma)$ with $|\mu_1 - \mu_2| < 2\sigma$ is compared to a best-fit obtained with $SGG(x, \mu, \sigma', 1, p)$, where $\mu = (\mu_1 + \mu_2)/2$ and $p > 2$. (b) $m_1N(x, \mu, \sigma_1) + m_2N(x, \mu, \sigma_2)$ is compared to a best-fit obtained with $SGG(x, \mu, \sigma, 1, p)$, where $p < 2$. In (c), $SGG(x, \mu, \sigma, q, p)$ is compared with $m_1N(x, \mu, \sigma_1) + m_2N(x, \mu, \sigma_2)$. Below each plot, the difference between the two functions is plotted in percent of the maximum value of these functions.

of Gaussian distributions on the one hand and a linear combination of *SGG* distributions on the other. Since finite mixture models with non-Gaussian coercivity distributions have not been reported in the literature, it is not possible to decide from a priori informations which kind of PDF should be used as a basis for a mixture model. From the mathematical point of view, all PDFs are equivalent, since the goodness of fit, which can be reached with a particular model, depends only upon the total number of parameters assumed, regardless of how they are assigned to individual components. Starting from these considerations, and from the fact that coercivity distributions of natural and artificial samples are nearly log-Gaussian, one could ask if the use of more complicated PDFs has any physical meaning. We will handle this problem in the following.

[31] To better understand the problem, we first illustrate the strong similarities that exist between a *SGG* distribution with $p \rightarrow 1$ and $q \rightarrow 2$ on one hand and a linear combination of two Gaussian distributions on the other. We consider three different situations, which are shown in Figure 10. In the first case, two Gaussian distributions with identical amplitudes and same σ, but slightly different values of μ, are fitted with a *SGG* distribution with $p = 1$ and $q > 2$. If $\Delta\mu/\sigma > 1$, where $\Delta\mu$ is the difference between

the means of the two Gauss distributions, the resulting function has two local maxima and is evidently bimodal. However, as $\Delta\mu/\sigma \rightarrow 0$, the resulting distribution becomes very similar to a slightly squared PDF ($k < 0$). In the second case, a *SGG* distribution with $q < 2$ is fitted to a linear combination of two Gaussian functions with the same μ but different values of σ. The two distributions converge to the same function for $q \rightarrow 2$. In the third case, a *SGG* distribution with $p \neq 1$ is fitted to a linear combination of two different Gaussian functions. Convergence of the two distributions is obtained for $|p| \rightarrow 1$. In all three cases, the *SGG* distribution and the combination of two Gaussian functions can be very similar. The possibility of distinguishing two overlapping Gaussian functions from a *SGG* distribution depends on the noise level of the data to be fitted and can be tested with a Pearson's χ^2 goodness of fit test. If the test is not passed, the fitting models are mathematically equivalent, but the corresponding interpretations are drastically different, since the number of inferred components is not the same. Generally, the use of more complicated PDFs for the end-member coercivity distributions has the effect of reducing the number of components needed to fit a measurement with a sufficient degree of precision. Two components with widely overlapping coercivity distributions may be modeled with one *SGG* distribution, and vice versa, a single component with $k \neq 0$ or $s \neq 0$ may be modeled with a combination of two Gaussian distributions. In both cases, incorrect interpretation may result. An example is given by the samples described in section 4.2, which contain magnetic components whose coercivity distribution are similar to the functions plotted in Figures 10b and 10c.

[32] If two overlapping PDFs cannot be resolved at the given confidence level, the sum of the estimated contributions may still be significant, despite the fact that the individual values of the estimates are not significant. In this case, the two PDF are conveniently modeled as a single component, eventually by substituting them with a more complex PDF. The use of PDFs with more distribution parameters, instead of a large number of distributions with fewer distribution parameters leads to results of the fitting model which are more stable against measurement errors. The stable behavior of a fitting with *SGG* distributions can be explained by the fact that small deviations from an ideal coercivity distribution, which arise from measurement errors, are taken into account by variations in skewness and kurtosis, rather than by variations in the contributions of the single components. Obviously, the values obtained for skewness and kurtosis may not be significant at all. A similar stability can be obtained with Gaussian functions if some of them are grouped as if they were one component. However, it is not always evident which distributions group together, and multiple solutions are often possible, as illustrated by the examples described in the following section.

4.2. Examples

[33] In this section, measurements of lake sediments and urban atmospheric particulate matter (PM) are presented.

4.2.1. Lake Sediments

[34] Lake sediment samples were taken from Baldeggersee, Switzerland. This lake is situated on the Swiss Plateau at 463 m asl, it has a surface area of 5.2 km^2 and a maximum water depth of 66 m. The catchment area (67.8 km^2) has been used intensively for agriculture since the nineteenth century. The lake was formed more than 15,000 years ago after the retreat of the Reuss glacier. Hills around the catchment area protect the lake from winds and facilitate oxygen depletion in deep waters. Several packets of varves indicate these depletion periods during the last 6000 years. The last and most severe eutrophication event started in 1885, triggered by the development of human activities in the catchment area. The depth to anoxic water column was 60 m in 1885 and rose to 10 m in 1970 [*Wehrli et al.*, 1997]. A 1.2 m long gravity core was taken in 1999 at the center of the lake and sampled every centimeter. The samples were immediately freeze dried to prevent oxidation and pressed into cylindrical plastic boxes. The core covers the last 200 years of sedimentation [*Wehrli et al.*, 1997]. Magnetite is the major magnetization carrier, with small amounts of a high-coercivity material, probably fine-grained hematite. The analysis of coercivity distributions is used here to separate the detrital component of the magnetic signal from the authigenic component (the magnetic particles produced by chemical and biological processes in the lake). In order to identify the detrital component, a sediment sample from a small river delta of the lake was taken. Since the catchment area is geologically and anthropogenically homogeneous all around the lake, this sample is expected to be representative of the detrital input. The sample was sieved in acetone in order to isolate the fraction <20 μm, which is the one that more easily reaches the center of the lake under normal conditions. In order to separate the individual contributions to the magnetic signal of the sediments and their variation during the last eutrophication event, AF demagnetization curves of ARM were measured on a selected number of samples distributed across the transition zone between the oxic and the anoxic part of the core. The same measurements were also performed on the sample taken from the river delta. After preliminary AF demagnetization with a 300 mT peak field, each sample was given an ARM using a 0.1 mT DC field and a 300 mT AF peak field. The samples were then stepwise AF demagnetized with increasing peak fields up to 300 mT. From each demagnetization curve, a coercivity distribution was calculated with CODICA (see section 2). Figure 11 shows detailed coercivity distributions and analyzed coercivity components of three samples, labeled G010, G044, and U03F. Sample G010 was taken at a depth of 11 cm from the most anoxic level of the gravity core, and sample G044 corresponds to a depth of 44.5 cm, far below the onset of eutrophication. Sample U03F is the <20 μm fraction of silt, collected from the small river delta. Different fitting models were used to analyze these samples; some results for G010 are summarized in Table 1. At least three magnetic components can be distinguished directly from the shape of the filtered coercivity distributions: a low-coercivity component (hereafter called component D), a component with intermediate coercivity values (component I) and a high-coercivity component which is not saturated at 300 mT (component H). In sample G044, the intermediate component seems to be composed of two PDFs with similar values of median destructive field.

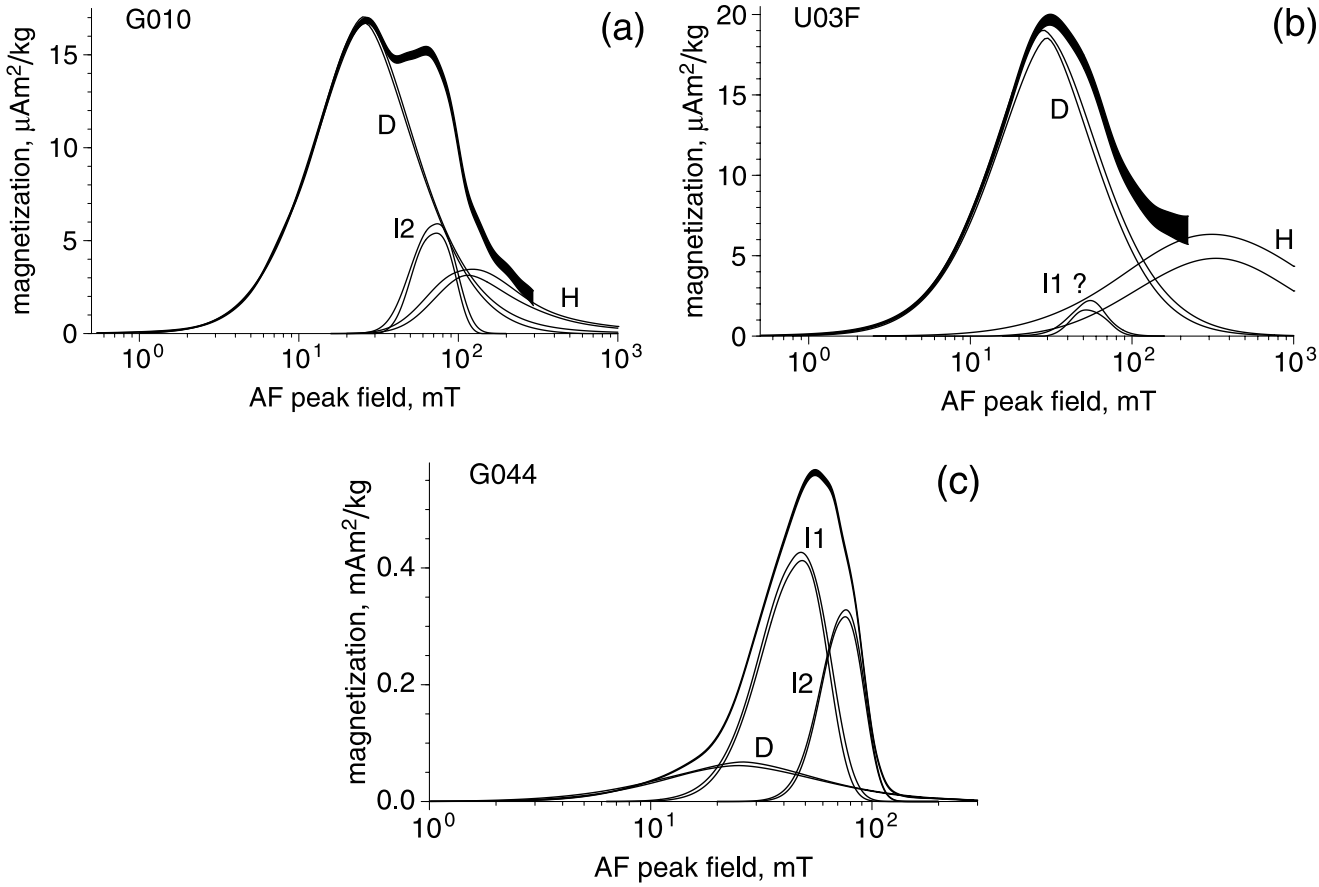

Figure 11. Example of integrated approach to the component analysis of coercivity distributions. (a) Coercivity distribution of a PM10 sample (GMA) collected in a green area near the city of Zurich (Switzerland). The thickness of the line is the standard deviation of the estimated error. The coercivity distribution is fitted with one *SGG* distribution. The difference between measured and fitted curve is plotted below (thick line) together with the measurement error estimation provided by CODICA (thin line pairs). The smallest error estimation refers to the real measurement of six demagnetization curves of ARM with 72 steps each. The largest error estimation is calculated for the measurement of one demagnetization curve with 12 steps. The intermediate error estimation refers to the measurement of six demagnetization curves with 12 steps each or one demagnetization curve with 72 steps. The modeled curve is incompatible with the highest precision measurement. Therefore, two magnetic components are used for the component analysis shown in (b). In this case, the coercivity distribution is well fitted within the error of the highest precision measurement. Line pairs represent the upper and lower limit for the coercivity distribution of each component. An alternative approach to high-precision measurements was the investigation of similar samples. In (c) and (d), the coercivity distributions of other two PM10 dust samples are shown. These samples were collected near a high-traffic road in the center of Zurich (WDK) and inside a highway tunnel near Zurich (GUH). The presence of two magnetic components (called N and A) is evident in these samples. Furthermore, the contribution of component A to the total ARM is related to the degree of pollution of the area (in increasing order: GMA, WDK, and GUH).

[35] Adequate mixture models are obtained with three or four *SGG* functions. Component H has generally low quality parameter estimates, because the available maximum field of 300 mT was not sufficient to saturate it. For each mixture model, a Pearson's χ^2 goodness of fit test was performed. The standard error of the distribution parameters was also estimated using the following procedure. An appropriate noise signal, which corresponds to the measurement error estimated by CODICA, was added to the coercivity distribution by means of a random number generator. The component analysis was then performed on the resulting distribution, and new values were obtained for each distribution parameter. The procedure was repeated many times (generally 100) in order to sample a significant set of estimates of the distribution parameters, which allow the calculation of the standard deviation for each parameter. The results are summarized in Table 2. Each end-member coercivity distribution can be normalized to have a unit saturation remanence and can be drawn separately, as shown in Figure 13. In this way, the comparison of end-member coercivity distributions is facilitated.

Table 1. Component Analysis of Sample G010 (Anoxic Lake Sediment) Based on the AF Demagnetization of an ARM Acquired in a 0.1 mT Bias Field[a]

Fitting PDF	χ^2 of Fitting ($\chi^2_{0.95}$)	Norm. Contrib. $\frac{m \pm \delta m}{M_{300mT}}$	MDF $\mu_2 \pm \mu_2$ mT	SD $\sigma_2 \pm \delta\sigma_2$	Skewness $\sigma \pm \delta\sigma$	Kurtosis $k \pm \delta k$	Comment
1 G	611 ± 35 (68.7)	0.812 ± 0.004	27.1 ± 0.1	0.358 ± 0.002	0	0	Significantly different
1 G		0.104 ± 0.005	75.3 ± 0.5	0.122 ± 0.002	0	0	from the measurements
1 G		0.088 ± 0.006	169 ± 6	0.23 ± 0.01	0	0	
Total		1.005 ± 0.003					
2 G	71 ± 22 (61.7)	0.63 ± 0.2	23 ± 2	0.33 ± 0.04	−0.09 ± 0.1	0.2 ± 0.1	Numerically unstable,
2 G		0.12 ± 0.02	71 ± 1	0.124 ± 0.006	−0.01 ± 0.06	−0.3 ± 0.1	single components are not real
1 G		0.27 ± 0.2	95 ± 50	0.35 ± 0.09	0	0	
Total		1.02 ± 0.003					
1 SGG	76 ± 20 (61.7)	0.79 ± 0.01	26 ± 1	0.38 ± 0.02	0.07 ± 0.2	0.5 ± 0.3	Numerically stable, slight deviations from
1 SGG		0.10 ± 0.01	69 ± 1	0.120 ± 0.004	−0.20 ± 0.06	−0.3 ± 0.1	Gaussian PDF, some are significant
1 SGG		0.14 ± 0.02	170 ± 10	0.40 ± 0.04	1.3 ± 0.3	3.5 ± 1	
Total		1.031 ± 0.006					
1 SGG	61 ± 20 (55.7)	0.77 ± 0.02	26 ± 1	0.38 ± 0.01	0.05 ± 0.1	0.5 ± 0.1	Numerically stable, slight deviations from
2 SGG		0.11 ± 0.04	72 ± 2	0.12 ± 0.01	0.1 ± 0.3	−0.4 ± 0.1	Gaussian PDF, some are significant
1 SGG		0.14 ± 0.04	130 ± 20	0.33 ± 0.06	0.2 ± 0.2	0.1 ± 0.4	
Total		1.019 ± 0.006					
Component 1		0.79 ± 0.01	26 ± 1	0.38 ± 0.02	0 ± 0.2	0.5 ± 0.2	c1: positive k
Component 2		0.11 ± 0.04	70 ± 2	0.12 ± 0.01	?	−0.4 ± 0.1	c2: probably 2 comp.
Component 3		0.14 ± 0.04	150 ± 20	0.36 ± 0.06	?	?	c3: not saturated
Total		1.03 ± 0.01					tot: 3% unsaturation

[a]The corresponding coercivity distribution has been plotted in Figure 11a. The following PDFs were assumed as end-member distributions: 3 Gaussian distributions, 5 Gaussian distributions, 3 *SGG* distributions, 4 *SGG* distributions. The second column gives the result of a Pearson's χ^2 goodness-of-fit test, and the other columns give the distribution parameters of the end-member coercivity distributions. The last row shows the final interpretation in terms of three components. Component 1 is characterized by a small MDF (μ_2 = 26 mT) and a significant positive kurtosis. Component 2 has an intermediate MDF, a small DP (σ_2 = 0.11), and a significant negative kurtosis. A negative kurtosis is characteristic for two overlapping components with similar values of μ_2. Component 3 is characterized by high values of the MDF and was not saturated at 300 mT.

[36] Models with <6 Gaussian PDFs do not fit the measured data sufficiently well. On the other hand, models with ≥6 Gaussian PDFs are not realistic, and the interpretation of each PDF in terms of magnetic components would be problematic. Models with three or four *SGG* distributions fit the measurements sufficiently well and provide significant estimates for, m, μ and σ of each component. Skewness and kurtosis are not significant for all components. However, the coercivity distribution of component D is similar to the function plotted in Figure 10b and shows consistent and systematic deviations from a Gaussian PDF: for all three samples $s = 0$ and $k \approx 0.5$, which corresponds to $p \approx 1.6$. The end-member coercivity distributions of the three samples are compared in Figure 13. The coercivity distributions of component D are identical within the measurement error in all three samples. The absolute contribution of this component varies moderately among the three samples, if compared with the contribution of the intermediate component. Thus, it is reasonable to assume that the magnetization of component D is carried by the same set of magnetic particles, whose magnetization is dominant in sample U03F, which should

Table 2. Summary of Distribution Parameters of the Magnetic Components Found in Samples G010, G044, and U03F From Baldeggersee, Switzerland

Parameter	U03F	G010	G044	Comment
$m \pm \delta m$, μA m^2/kg	16 ± 0.6	14 ± 0.2	59 ± 3	**Detrital soft component:**
100 $(m \pm \delta m)/M_{rs}$	67 ± 3	77 ± 1	20 ± 1	μ_2, σ_2, s, and k are almost identical
$\mu_2 \pm \delta\mu_2$, mT	29 ± 1	26 ± 1	25.5 ± 0.5	
$\sigma_2 \pm \delta\sigma_2$	0.389 ± 0.006	0.38 ± 0.02	0.40 ± 0.01	
$s \pm \delta s$	0 ± 0.08	0 ± 0.1	0 ± 0.002	
$k \pm \delta k$	0.54 ± 0.04	0.5 ± 0.2	0.42 ± 0.05	
$m \pm \delta m$, μA m^2/kg	7.3 ± 0.6	2.5 ± 0.7	1.8 ± 0.6	**Hard component:**
100 $(m \pm \delta m)/M_{rs}$	30 ± 3	14 ± 2	0.6 ± 0.2	significant differences in all parameters.
$\mu_2 \pm \delta\mu_2$, mT	320 ± 50	150 ± 20	180 ± 20	
$\sigma_2 \pm \delta\sigma_2$	0.52 ± 0.05	0.36 ± 0.06	0.18 ± 0.03	
$m \pm \delta m$, μA m^2/kg	6 ± 3		59 ± 3	**Intermediate component 1:**
$\mu_2 \pm \delta\mu_2$, mT	54 ± 2		41.8 ± 0.5	Relatively soft. Small DP.
$\sigma_2 \pm \delta\sigma_2$	0.11 ± 0.02		0.153 ± 0.002	Maybe not the same component in U03F and G044.
$s \pm \delta s$	?		−0.55 ± 0.04	
$k \pm \delta k$	?		0.33 ± 0.08	
$m \pm \delta m$, μA m^2/kg		1.9 ± 0.3	77 ± 4	**Intermediate component 2:**
$\mu_2 \pm \delta\mu_2$, mT		70 ± 2	71.3 ± 0.6	Relatively hard. Very small DP. μ_2 and σ_2 are almost identical.
$\sigma_2 \pm \delta\sigma_2$		0.12 ± 0.01	0.095 ± 0.002	
$s \pm \delta s$		?	−0.41 ± 0.04	
$k \pm \delta k$		−0.4 ± 0.1	0.14 ± 0.07	

Table 3. Summary of Distribution Parameters of the Magnetic Components Found in PM10 Samples

Parameter	GMA	WDK	GUH	Comment
$m \pm \delta m$, μA m^2/kg	338 ± 2	590 ± 2	316 ± 5	**Natural mineral dust (N):**
100 $(m \pm \delta m)/M_{rs}$	73 ± 1	41 ± 1	31 ± 1	Coercivity distributions of GMA and WDK are similar.
$\mu_2 \pm \delta\mu_2$, mT	23.8 ± 0.1	19.6 ± 0.1	15.9 ± 0.3	GUH was collected in a tunnel.
$\sigma_2 \pm \delta\sigma_2$	0.456 ± 0.001	0.438 ± 0.001	0.343 ± 0.01	
$s \pm \delta s$	−0.58 ± 0.02	−0.65 ± 0.01	−1.05 ± 0.03	
$k \pm \delta k$	0.76 ± 0.01	0.928 ± 0.001	1.756 ± 0.02	
$m \pm \delta m$, μA m^2/kg	128 ± 2	864 ± 2	709 ± 2	**Vehicle pollution dust (A):**
100 $(m \pm \delta m)/M_{rs}$	27 ± 1	59 ± 1	69 ± 1	All coercivity distributions are similar.
$\mu_2 \pm \delta\mu_2$, mT	77.3 ± 0.2	74.7 ± 0.2	77.5 ± 0.3	
$\sigma_2 \pm \delta\sigma_2$	0.245 ± 0.001	0.275 ± 0.001	0.23 ± 0.01	
$s \pm \delta s$	−0.20 ± 0.02	−0.65 ± 0.01	−0.2 ± 0.1	
$k \pm \delta k$	−0.19 ± 0.01	0.785 ± 0.002	−0.12 ± 0.01	

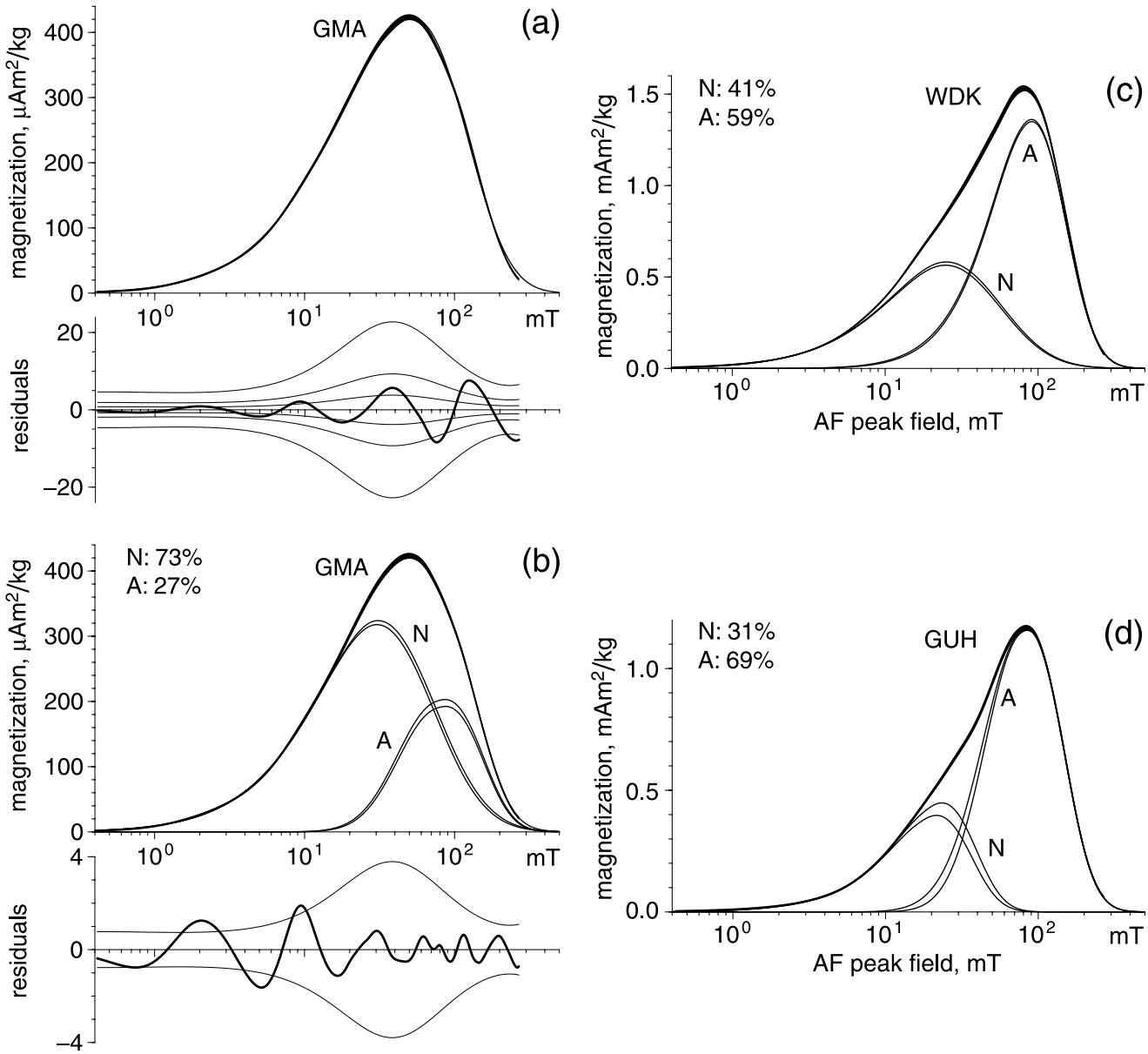

Figure 12. Finite mixture model for the three sediment samples presented in this paper. The solid line represents the coercivity distribution of the sample. The thickness of the line being the standard deviation of the estimated error. The other line pairs represent the upper and lower limit for the coercivity distributions of each identified component (labeled with D, I, and H). Details of the component analysis for the three samples are listed in Table 2.

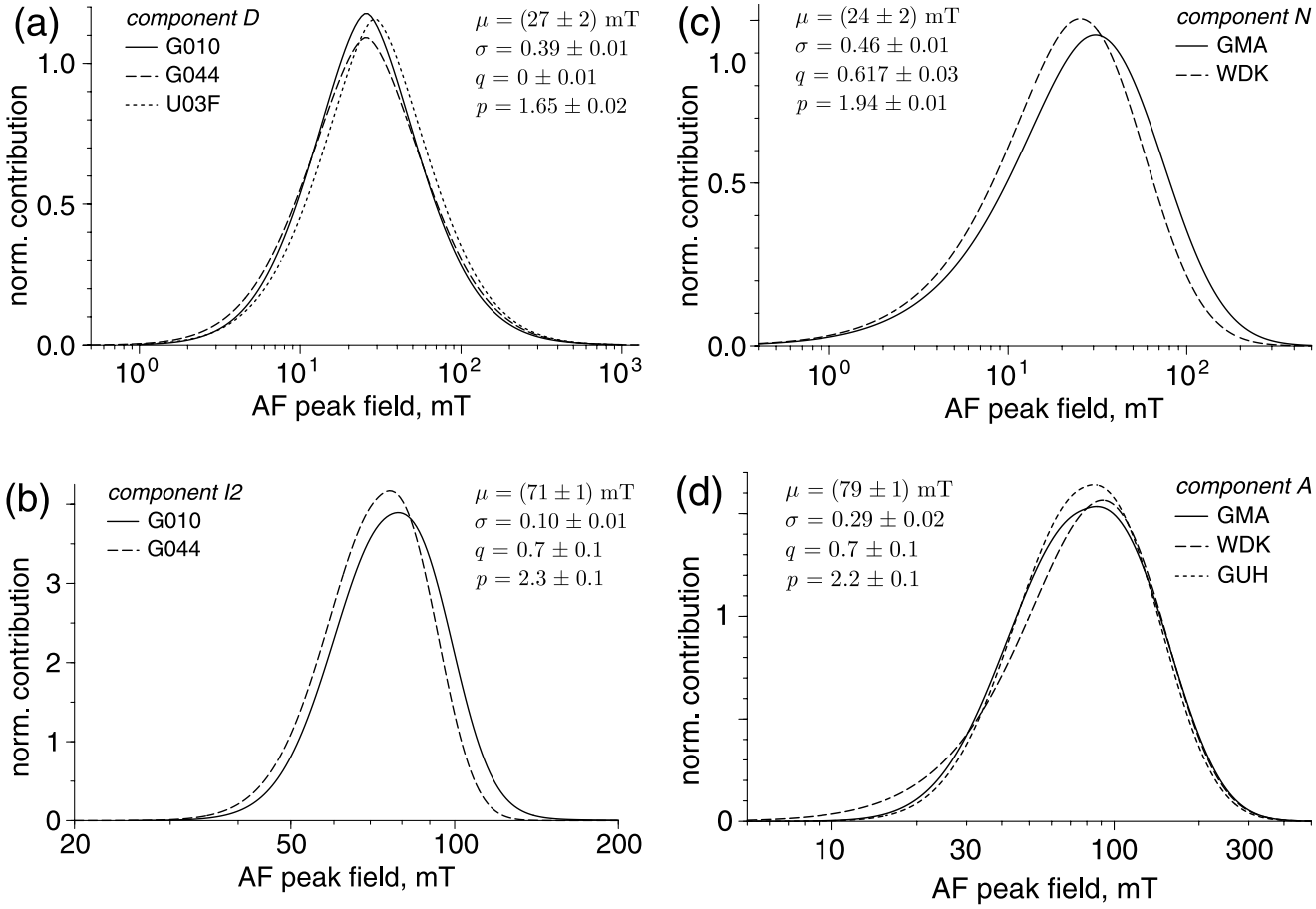

Figure 13. Coercivity distributions of the magnetic components found in the samples analyzed in this paper. The coercivity distributions are normalized so that the saturation remanence (area under the curve) equals to 1 to facilitate the comparison between different samples. (a) Component D of lake sediment samples G010, G044, and U03F. The coercivity distribution of this component is identical in all three samples within the confidence levels given by the measurement errors. This component may represent detrital particles transported toward the center of the lake. (b) Component I2 of lake sediment samples G010 and G044. The coercivity distribution of this component is identical in both samples within the confidence levels given by the measurement errors. The relatively high coercivity and the extremely small value of σ are indicative for intact magnetosomes, either isolated or arranged in chains. (c) Component N of the PM10 samples GMA and WDK. The coercivity distribution of this component is slightly different in the two samples. This component may represent the magnetic minerals contained in the mineral part of natural dust. (d) Component A of PM10 samples GMA, WDK, and GUH. This component may represent the magnetic minerals associated with the pollution products of motor vehicles.

be representative for the detrital input into the lake. Component I has extremely low values of the dispersion parameter: $\sigma < 0.15$. In the sample with strongest magnetization (G044) it is evident that component I is composed by at least two subcomponents, which can be found individually in the other samples at lower concentration. The magnetization of component I varies from 6 μA m^2/kg in U03F (2.6% of the bulk magnetization) to 136 μA m^2/kg in G044 (80% of the bulk magnetization). The coercivity distribution of component I is comparable to that of samples containing intact cells of magnetotactic bacteria [*Moskowitz*, 1988]. Intact and broken chains of magnetosomes were observed under the electron microscope in sample G044. Therefore component I is identified as magnetite grains of bacterial origin. The magnetic signal of component I may reflect changes in the production rate of biogenic magnetite or a possible reductive dissolution process of fine magnetite grains during eutrophication periods. Component H is badly resolved, because saturation was not reached in any of the three samples. The highest contribution of this component is found in sample U03F. The parameters μ and σ of components D, I, and H in all three samples are drawn in a scatterplot in Figure 14. The three components are well grouped in three different regions of the plot. Component I is compatible with the magnetic properties of pure single-domain magnetite, whereas component D contains a small but significant amount of magnetic particles with coerciv-

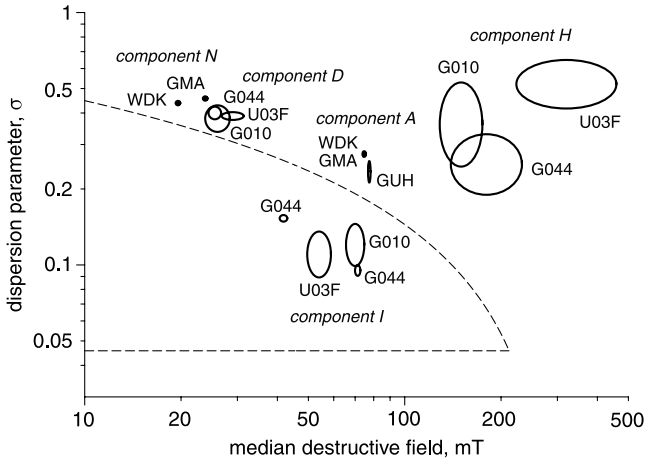

Figure 14. Summary of the mean properties of the magnetic components found in the samples presented in this paper. For each component, the median destructive field and the dispersion parameter have been plotted. The ellipses indicate the standard deviation of the estimated errors. The dashed line delimitates the range of values of the MDF and the DP for pure magnetite. The lower limit for the DP is defined by the coercivity distribution of a set of identical, uniaxial, and randomly oriented magnetite particles according to the Stoner-Wolfarth model. The upper limit is defined by all coercivity distributions that reach 99% saturation at 300 mT.

ities >300 mT, probably representing oxidized magnetite. Component H is associated with a magnetically hard mineral.

4.2.2. Urban Atmospheric PM

[37] Urban atmospheric PM is the subject of several studies because of its negative effects on human health [*Harrison and Yin*, 2000]. Magnetic properties of urban PM have been recently investigated by several authors [e.g., *Shu et al.*, 2001; *Muxworthy et al.*, 2002] because of the high concentration of magnetic minerals in urban pollution. The identification of various sources of magnetic particles in urban PM would be of great interest for environmental studies. Three samples of urban PM <10 μm (called PM10 in the following) were taken in the region of Zurich (Switzerland) with a high-volume air sampler DIGITEL DHA-80. Each sample was taken during a 24 hour run by pumping 720 m^3 of air through a filter. All samples were taken during summer 2001 under dry weather conditions. Heavy industries are absent from the region, and the heating systems of buildings were not working during that period. Under these conditions, the major sources of urban PM in the city center of Zurich are represented by motor vehicles and waste combustion products [*Hüglin*, 2000].

[38] Sample GMA was taken in a green area adjacent to our paleomagnetic laboratory outside the city of Zurich. The area is located far away from any heavily traveled road and a small amount of urban pollution is therefore expected to be found in this sample. The measured daily mean PM10 concentration was 14 $\mu g/m^3$. Sample WDK was taken in the city center of Zurich near a heavily traveled road (Wiedikon). The daily mean PM10 concentration was 66 $\mu g/m^3$, and a large amount of pollution produced by motor vehicles is expected. Sample GUH was taken inside a 3.5 km long highway tunnel near Zurich (Gubrist tunnel). The pollution by motor vehicles is expected to be highest in this sample, with a daily mean PM10 concentration of 91 $\mu g/m^3$. The samples were measured with the same procedure as the lake sediments. Results of the component analysis are summarized in Table 3 and the coercivity distributions are plotted in Figure 12. The coercivity distribution of the GMA sample is similar to the distribution plotted in Figure 10c, and it is well fitted with one *SGG* function. This fitting would pass a significance test with the measurement results of a common AF demagnetization experiment. However, two components are needed to model the results of a high-precision measurement consisting in six stacked AF demagnetization curves with 72 steps each. The GMA sample can be considered as an experimental example of the interpretation problems discussed in section 4.1.

[39] The presence of two magnetic components in the WDK and GUH samples is evident already from a visual inspection of the coercivity distributions calculated with CODICA. The contribution of the component with higher coercivity (component A in the following) to the total magnetization is related to the amount of urban pollution in the sampling area. Therefore, we identify component A with the urban PM. The component with smaller coercivity (component N) shows the opposite trend and can be associated to the magnetic minerals contained in natural dust. The coercivity distributions of components A and N are plotted separately in Figures 13c and 13d; and the corresponding distribution parameters are plotted in Figure 14.

5. Conclusions

[40] The component analysis of coercivity distributions offers a way to estimate the contribution of different magnetic materials to the total magnetization of a sample. Component analysis is very sensitive to measurement errors and to the shape of the function used to model the end-member distributions. Nevertheless, it allows to discriminate and quantify different magnetic components of the same mineral, a result that is impossible to achieve with standard rock magnetic investigations based on bulk measurements. Careful experimental design and data treatment allow to reduce the effect of measurement errors into acceptable limits. Unjustified constrains on the shape of the model functions used for component analysis should be avoided. For this reason, generalized distribution functions have been introduced, which are able to fit a large number of different statistical distributions. In this way, a precise estimation of magnetite components with widely overlapped coercivity distributions was possible on lake sediments. Different aspects related to the calculation and the interpretation of coercivity distributions were analyzed and tested on synthetic and natural coercivity distributions. The results of these tests can be summarized into the following points:

1. Not all end-member coercivity distributions can be modeled using a logarithmic Gaussian function. General-

ized distributions with five parameters can take into account variations in the symmetry (skewness) and the curvature (kurtosis). End-member coercivity distributions with significant and systematic deviations from a logarithmic Gaussian function are needed to interpret theoretical AF demagnetization curves of single-domain and multidomain magnetite, as well as measured demagnetization curves of synthetic samples containing sized magnetite grains.

2. The significance of the component analysis of coercivity distributions should be evaluated with statistical tests and with an error estimation of each distribution parameter. Analytical expressions for the error estimations have been developed.

3. Multiple solutions for the component analysis are possible. In this case, other informations are needed to identify the correct solution. A comparison between the component analysis of different sediments, which belong to the same ecological system, is useful for the identification of magnetic components.

4. Component analysis is applicable to large sets of samples with standard precision measurements, providing the number of magnetic components and their coercivity distribution parameters is known from detailed measurements on a selection of few, adequate reference samples.

Appendix A: Error Calculations

Table A1. Effect of Different Measurement Error Sources on the Calculation of a Coercivity Distribution[a]

Error Source	Magnetization Curve	Coercivity Distribution
General, h = $H/\Delta H$	$M_i = M(H_i) + \Delta M$ ΔM = total error	$f_i = \frac{H_{i+1}+H_i}{2}\frac{M_{i+1}-M_i}{H_{i+1}-H_i}$
Measurement error: δM Applied field error: δH	$(\Delta M)^2 = (\delta M)^2 + f^2(\delta H)^2$	$(\Delta f)^2 = 2h^2(\delta M)^2 + 2f^2(\delta H)^2$
Absolute measurement error: $dM = \varepsilon$	$\Delta M = \varepsilon$	$\Delta f = \sqrt{2}h\varepsilon$
Relative measurement error: $\delta M/M = \varepsilon$	$\Delta M/M = \varepsilon$	$\Delta f = \sqrt{2}h\varepsilon M$
Absolute applied field error: $\delta H = \varepsilon$	$\Delta M = \varepsilon f$	$\Delta f/f = \sqrt{2}h\varepsilon/H$
Relative applied field error: $\delta H/H = \varepsilon$	$\Delta M = \varepsilon f H$	$\Delta f/f = \sqrt{2}h\varepsilon$
Mechanical instability: $\delta M = \varepsilon HM$	$\Delta M = \varepsilon HM$	$\Delta f = \sqrt{2}h\varepsilon HM$

[a]The numerical calculation of a coercivity distribution from an acquisition/demagnetization curve with finite differences is given in the first row. In the second row, general equations for the error estimation are given by assuming an error δM in the measurement of the magnetization M and an error δH in the applied field H. In the other rows, error estimations are given for particular cases where the absolute or the relative error of M or H are described by a white noise of amplitude ε. The last row gives an error estimation in the case where a small part ε of all magnetic particles, which are not magnetically unblocked by the applied field, becomes mechanically unstable and rotates under the influence of a torque $T \propto H$. The amount of these particles is assumed to be proportional to T and thus to H. The corresponding magnetization is then proportional to $HM(H)$, where $M(H)$ is the magnetization of all magnetically blocked particles.

Appendix B: A Short Guide to CODICA

[41] The elaboration of an acquisition/demagnetization curve with CODICA consists in the following steps.

B1. Data Checking

[42] The measurement curve is always displayed as a demagnetization curve (Figure 3a): this does not affect the calculation of the coercivity distribution. The user is asked to enter an estimation of the measurement error (if known). This estimate may come from inspection of the measurement curve and/or experimental experience with the instruments used. A combination of a relative and an absolute error is assumed to affect the measurements and the AF field. Systematic errors, like magnetization offsets and temperature effects on the sample and on the AF coil do not affect significantly the shape of the measured curve and may not be included. The calculation of a coercivity distribution and the related error is independent of the error estimate entered by the user. This first estimate is needed by the program in order to display a rough estimation of the confidence limits of the measured curve, which should help the user through the following steps of the program.

B2. Scaling the Magnetic Field (Figure 3b)

[43] As discussed in section 2.2, an acquisition/demagnetization curve is supposed to have a sigmoidal shape on a logarithmic field scale. However, the measured curves are not symmetrical. Often, they show a long tail at high fields. In case of lognormal coercivity distributions, the measured curve represented on a logarithmic field scale becomes symmetric. In all other cases the curve is asymmetric on both a linear and a logarithmic field scale. An appropriate scale change which offers a set of intermediate scales between linear and logarithmic is defined by the power function $H^* = H^p$, p being a positive exponent. An appropriate value of p is chosen, so that the scaled curve reaches maximum symmetry. The symmetry of the curve is compared with a reference sigmoidal curve, expressed by an analytical function (a tanh function in our program). The scaled curve is therefore represented together with the best fitting tanh function. An automatic routine optimizes the scaling exponent p so that the difference between the original curve and the model curve is minimal.

B3. Scaling the Magnetization (Figure 3c)

[44] A tanh function was chosen as a reference in order to scale the field, because of its mathematical simplicity. It does not have a particular meaning and any other similar function could be used instead. If the measured curve $M(H)$ coincides with a tanh function, the application of the inverse function arctanh to the magnetization values generates a linear relation between scaled field and scaled magnetization. The scale transformation applied to the magnetization values is based on the following model for the relationship between the scaled field H^* and the measured magnetization $M(H^*)$ in a demagnetization curve:

$$M(H^*) = M_{rs}\left[1 - \tanh\left(a\left(H^* - H^*_{1/2}\right)\right)\right] + M_0 \qquad \text{(B1)}$$

Table A2. A Summary of Properties of the *SGG* Distribution and the Relative Error Estimations[a]

Distribution Properties	Relation With the Distribution Parameters	RCF Inequality	Minimum χ^2 Fitting (One Unknown Parameter)
Optimized $\chi^2(\theta)$:	$n - l - 1$		
α confidence limits:	$[\chi_{n-l-1;\alpha}, \chi_{n-l-1;1-\alpha}]$		
for $n - l \gg 1$:	$(n-l) \pm u_\alpha\sqrt{2(n-l)}$		
General parameter θ		$\Delta\theta \geq \frac{\sqrt{2}\pi^{1/4}\delta y\sqrt{\sigma\Delta x}}{\left[\int_{-\infty}^{\infty}\left(\frac{\partial f(x)}{\partial\theta}\right)^2\frac{dx}{f(x)}\right]^{1/2}}$	$\Delta\theta = \frac{\delta y\sqrt{\Delta x}}{\left[\int_{-\infty}^{\infty}\left(\frac{\partial f(x)}{\partial\theta}\right)^2 dx\right]^{1/2}}$
Amplitude m		$\delta m \geq \sqrt{2}\pi^{1/4}\delta y\sqrt{\sigma\Delta x}$	$\delta m = \sqrt{2}\pi^{1/4}\delta y\sqrt{\sigma\Delta x}$
Mean $\mu_2 = E(x)$	$\mu + \frac{s}{6}(1 + 0.856k)$	$\delta\mu_2 \geq \sqrt{2}\pi^{1/4}\frac{\delta y}{m}\sqrt{\sigma^3\Delta x}$	$\delta\mu_2 = 2\pi^{1/4}\frac{\delta y}{m}\sqrt{\sigma^3\Delta x}$
SD: $\sigma_2^2 = E[(x-\mu_2)^2]$	$\sigma^2(1 + 1.856k)(1 - \lvert s\rvert/3)$	$\delta\sigma_2 \geq \pi^{1/4}\frac{\delta y}{m}\sqrt{\sigma^3\Delta x}$	$\delta\sigma_2 = 2\sqrt{23}\pi^{1/4}\frac{\delta y}{m}\sqrt{\sigma^3\Delta x}$
Skewness s: $E[(x-\mu_2)^3]/\sigma_2^3$	$-6\ \mathrm{sgn}\ q\ (1-q)2\ (1 + 1.856k)$	$\delta s \geq 4(2\pi)^{1/4}\frac{\delta y}{m}\sqrt{\sigma\Delta x}$	$\delta s = \frac{48}{\sqrt{13}}\pi^{1/4}\frac{\delta y}{m}\sqrt{\sigma\Delta x}$
Kurtosis k: $E[(x-\mu_2)^4]/\sigma_2^2 - 3$	$2 - p$	$\delta k \geq 3.204\frac{\delta y}{m}\sqrt{\sigma\Delta x}$	$\delta k = 8.243\frac{\delta y}{m}\sqrt{\sigma\Delta x}$

[a]The following notations are used: n is the number of measurements, l the number of estimated parameters, and u_α the α-quantile of the standardized Gaussian distribution ($u_{0.95} = 1.6$). Other notations are explained in the text. The second column gives approximate estimations of some distribution properties when $p \to 1$ and $q \to 2$. The third column gives the minimum error estimations of all distribution parameters, according to the RCF inequality. The last column gives the error estimations of the minimum χ^2 fitting method, when only one parameter is unknown.

where M_{rs} has the physical meaning of a saturation remanence (if the measured curve is saturated at the highest field value), M_0 has the physical meaning of a residual magnetization ($M_0 = 0$ if saturation can be reached), $H^*_{1/2}$ is the scaled median destructive field, and a is a parameter that controls the steepness of the curve. The following scale transformation

$$M^* = \mathrm{artanh}\left(1 - \frac{M - M_0}{M_{\mathrm{rs}}}\right) \tag{B2}$$

generates the linear relation $M^* = a(H^* - H^*_{1/2})$ between scaled field and scaled magnetization. The four parameters M_{rs}, $H^*_{1/2}$, M_0, and a have to be chosen in a way that the scaled magnetization curve as linear as possible. The program optimizes the parameters $H^*_{1/2}$ and a automatically using a Levenberg–Marquard algorithm for nonlinear fitting. The parameters M_0 and $M_0 + M_{rs}$ represent the asymptotic values of the magnetization curve. Their optimization is controlled by the user, since it was found that the optimization is very unstable with respect to these parameters. The scaled curve is represented together with a least squares linear fitting. Deviation from the least squares line can be minimized with an appropriate choice of M_0 and $M_0 + M_{rs}$. In general, too small values of M_0 or too high values of $M_0 + M_{rs}$ produce a flattening at the right and left end of the scaled curve, respectively. In contrast, too high values of M_0 or too small values of $M_0 + M_{rs}$ produce a steepening of the scaled curve at the right and left end of the scaled curve, respectively. Random deviations from the least squares line indicate the presence of measurement noise, systematic smooth deviations indicate a divergence of the measured curve from (B1). Best results are achieved using samples in which one magnetic component is dominant or in which different components have a wide range of overlapping coercivities. In both cases the choice of 5 independent parameters for the two scaling operations (p, M_{rs}, $H^*_{1/2}$, M_0, and a) is sufficient to achieve an excellent linear relationship between scaled field and scaled magnetization. In case of populations with drastically different coercivity ranges (i.e., magnetite and hematite) the scaling method is less effective, but in this case the separation of the different components is also less critical and can be performed even directly on the measured curve.

B4. Plotting the Residuals (Figure 3d)

[45] Once the measured curve is scaled with respect to field and magnetization, the deviation of the scaled curve from the least squares line is plotted. We will call this

Table A3. Summary of Error Estimations for the Parameters of a *SGG* Distribution[a]

Distribution Moments	Minimum χ^2 Fitting (With $l = 1$)	Num. Est. ($l = 1$)	Minimum χ^2 Fitting (With $l = 3$)	Num. Est. ($l = 3$)	Num. Est. ($l = 5$)
Amplitude m	$\delta m = \sqrt{2}\pi^{1/4}\delta y\sqrt{\sigma\Delta x}$	0.993	$\delta m = \sqrt{3}\pi^{1/4}\delta y\sqrt{\sigma\Delta x}$	1.203	1.293
Mean μ_2	$\delta\mu_2 = 2\pi^{1/4}\frac{\delta y}{m}\sqrt{\sigma^3\Delta x}$	0.990	$\delta\mu_2 = 2\pi^{1/4}\frac{\delta y}{m}\sqrt{\sigma^3\Delta x}$	1.021	1.032
SD σ_2	$\delta\sigma_2 = \sqrt{\frac{8}{3}}\pi^{1/4}\frac{\delta y}{m}\sqrt{\sigma^3\Delta x}$	0.997	$\delta\sigma_2 = \pi^{1/4}\frac{\delta y}{m}\sqrt{\sigma^3\Delta x}$	1.139	2.643
Skewness s	$\delta s = \frac{48}{\sqrt{13}}\pi^{1/4}\frac{\delta y}{m}\sqrt{\sigma\Delta x}$	0.883			1.411
Kurtosis k	$\delta k = 8.243\frac{\delta y}{m}\sqrt{\sigma\Delta x}$	0.698			2.032

[a]The errors are calculated analytically and numerically for the minimum χ^2 fitting method. The numerical error estimation is obtained by fitting 1000 simulated *SGG* distributions. These distributions are obtained by adding a Gaussian noise signal of known amplitude to a standardized *SGG* distribution ($m = 1$, $\mu = 0$, $\sigma = 1$, $q = 1$, and $p = 2$). The numerical estimates are reported as the ratio between the results of the numerical simulation and the analytical equations reported in the second column. The second and the third columns refer to a minimum χ^2 fitting with one unknown parameter (m, μ, σ, q, or p), the fourth and fifth columns to a minimum χ^2 fitting with three unknown parameters (m, μ, and σ), and the last column to a minimum χ^2 fitting where all parameters are unknown.

deviation the residuals curve. At this step, measurement errors are enormously enhanced, as can be seen by comparing the residuals with the original measured curve (not shown in Figure 3d). The estimated maximum measurement error is plotted in the form of a band around the residual curve. If the error estimation entered by the user was correct, the amplitude of the random oscillations of the residual curve should show the same order of magnitude as the displayed errors.

B5. Scaling the Residuals (Figure 3e)

[46] Generally, the residuals generate a sinusoidal curve, which is more or less "quenched" at one end. As in step 2, the field axis can be rescaled with a power transformation in order to approach a quite regular sinusoidal curve, which later can be filtered in a more effective way. After this new rescaling step, the residual curve is almost sinusoidal. Its Fourier spectrum is concentrated in a narrow band around a dominant wavelength, so that a simple low-pass filter would easily remove the high-frequency measurement noise.

B6. Filtering the Residuals (Figure 3f)

[47] The residual curve is now ready to be filtered in order to remove the measurement noise. The filter applied by the program is a modified Butterworth low-pass filter, defined by:

$$F(\nu) = \frac{1}{\left(1 + \nu_0^b/\nu^b\right)^{1/2b}} \tag{B3}$$

where ν is the frequency of the spectrum, ν_0 the so-called cutoff frequency, and b^3 1 the order of the filter. The filter parameters ν_0 and b are chosen by the user. Details of the residual curve with an extension smaller than $1/\nu_0$ on the field axis are filtered out. The sharpness of the filter is controlled by its order b: $b \rightarrow \infty$ gives a cutoff filter. The filter parameters should be chosen so that the measurement error is suppressed without changing the global shape of the curve. This condition is met by choosing the smallest value of ν_0, by which the difference between the filtered and the unfiltered curve attains the same maximal amplitude as the estimated measurement errors. The choice of larger values of ν_0 leads to a coercivity spectrum that fits the measured curve better but still contains an unremoved component of the measurement errors. The choice of larger values of ν_0 may produce a change in the shape of the curve and suppress significant details.

B7. Calculating the Filtered Demagnetization Curve

[48] Now, the filtered residuals are converted back to the original curve by applying the steps 2–5 in reverse order. The result is a demagnetization curve, which is supposed to be free of measurement errors.

B8. Calculating and Plotting the Coercivity Distribution

[49] The filtered demagnetization curve obtained at point 7, the coercivity distribution is calculated as the absolute value of the demagnetization curve. The user can choose between a linear, a logarithmic and a power field scale. The maximum amplitude of the error of the coercivity distribution is estimated in the program by comparing the measurement curve with the filtered curve. The error estimation is displayed as an error band on the plot (Figure 1).

Appendix C: Error Estimation

[50] A measured distribution is given by $y_i = f(x_i) + \delta y_i$, where (x_i, y_i) is a measurement point and δy_i the related measurement error. In following we assume the measurement error to be ergodic (i.e., statistically independent of x)

C1. The RCF Theorem

[51] Let $f(x|\theta)$ be a PDF with distribution parameter θ, and $X_1, \ldots, X_N$ a set of N realizations of the statistic variate X. The variance var $\hat{\theta}$ of the parameter $\hat{\theta}$ estimated with this set of realizations obey the RCF inequality [*Cowan*, 1998]:

$$\mathrm{var}\left(\hat{\theta}\right) \geq \frac{1}{N \sum_{i=1}^{N} f(x_i|\theta)[\,\partial_\theta \ln f(x_i|\theta)]^2} \tag{C1}$$

We use the RCF inequality to calculate var $\hat{\theta}$ when $f(x|\theta)$ is measured directly, instead of $X_1, \ldots, X_N$. For this propose, we imagine that $f(x|\theta)$ is calculated from a set of N realizations by counting the numbers N_i of realizations which belong to given intervals of amplitude Δx_i around a set of reference points $x_1, \ldots, x_n$. Consequently, $y_i = N_i/\Delta x_i$ and $y_i \rightarrow f(x_i|\theta)$ for $N \rightarrow \infty$, $\Delta x_i \rightarrow 0$. The probability distribution of N_i is a Poisson distribution with expected value $E(N_i) = Nf(x_i)\Delta x_i$ and variance $\mathrm{var}(N_i) = E(N_i)$. Because $\mathrm{var}(N_i)/E^2(N_i) = \mathrm{var}\,\delta y_i/y_i^2$, we obtain $E(N_i) = y_i^2/\mathrm{var}\,\delta y_i$. Inserting the sum of all N_i into (C1) gives:

$$\mathrm{var}\left(\hat{\theta}\right) \geq \frac{1}{\sum_{i=1}^{n} \left(\frac{y_i}{\mathrm{var}\delta y_i}\right)^2 \sum_{i=1}^{n} \frac{[\partial_\theta f(x_i|\theta)]^2}{f(x_i|\theta)}} \tag{C2}$$

For equally spaced reference points, $x_{i+1} - x_i = \Delta x$, and if $\Delta x \rightarrow 0$ the summands in (C2) are conveniently replaced by integrals:

$$\mathrm{var}\left(\hat{\theta}\right) \geq \frac{\Delta x}{\int_{-\infty}^{\infty} \frac{f^2(x|\theta)}{\mathrm{var}\delta y(x)}\,\mathrm{d}x \int_{-\infty}^{\infty} \frac{[\partial_\theta f(x|\theta)]^2}{f(x|\theta)}\,\mathrm{d}x} \tag{C3}$$

A further simplification is obtained by assuming the measurement error δy_i to be ergodic. Then, $\mathrm{var}\,\delta y_i = (\delta y)^2$ and:

$$\mathrm{var}\left(\hat{\theta}\right) \geq \frac{\Delta x(\delta y)^2}{\int_{-\infty}^{\infty} f^2(x|\theta)\mathrm{d}x \int_{-\infty}^{\infty} \frac{[\partial_\theta f(x|\theta)]^2}{f(x|\theta)}\,\mathrm{d}x} \tag{C4}$$

If $f(x|\theta)$ is a Gauss distribution with variance σ^2, simplifies finally to (8).

C2. Error Estimation With Unbiased Fitting Methods

[52] Both the maximum likelihood (ML) and the minimum χ^2 fitting method are asymptotically identical and absolute efficient for $n \rightarrow \infty$, where n is the number of measured points [*Cowan*, 1998]. We handle therefore only the minimum χ^2 method, which is directly related to the Pearson's χ^2 goodness of fit test (see section 2.3). Consider a set of N realizations $X_1, \ldots, X_N$ of the statistic variate X,

and a model distribution $f(x|\boldsymbol{\theta})$ which depends on the distribution parameters $\boldsymbol{\theta} = (\theta_1, \ldots, \theta_k)$. The χ^2 estimator is given by:

$$\chi^2(\boldsymbol{\theta}) = \sum_{i=1}^{n} \frac{[N_i - \Delta x_i f(x_i|\boldsymbol{\theta})]^2}{\Delta x_i f(x_i|\boldsymbol{\theta})} \tag{C5}$$

where N_i is the number of realizations which belong to an interval of amplitude Δx_i around a given value x_i. The minimum χ^2 estimate $\hat{\boldsymbol{\theta}}$ is the value of θ which minimizes $\chi^2(\boldsymbol{\theta})$. In our case, the individual realizations are unknown, but a measure of $f(x, \boldsymbol{\theta})$ is given. As shown before, each measurement y_i of $f(x_i, \boldsymbol{\theta})$ is related to a number $n_i = y_i^2/\text{var}\,\delta y_i$ of realizations. In this case, (C5) can be written as:

$$\chi^2(\boldsymbol{\theta}) = \sum_{i=1}^{m} \frac{[y_i - f(x_i|\boldsymbol{\theta})]^2}{\text{var}\,\delta y_i} \tag{C6}$$

If the measurement error is ergodic, $\text{var}\,\delta y_i = (\delta y)^2$ and (C6) simplifies to:

$$\chi^2(\boldsymbol{\theta}) \cong \frac{1}{(\delta y)^2} \sum_{i=1}^{m} [y_i - f(x_i|\boldsymbol{\theta})]^2 \tag{C7}$$

Equation (C7) is proportional to the mean quadratic error, and the χ^2 fitting method converge to a simple least squares fitting. It should be noted that this result holds only as far as $\delta y(x)$ is independent of x, and $|\delta y_i| \ll f(x_i|\boldsymbol{\theta})$. If for instance the relative error $\delta y_i/y_i$ is ergodic instead of δy_i, $\chi^2(\boldsymbol{\theta})$ is no longer related to the mean quadratic error. The minimization of $\chi^2(\boldsymbol{\theta})$ is performed by setting:

$$\partial\chi^2(\boldsymbol{\theta})/\partial\theta_i = 0 \quad , i = 1 \ldots k \tag{C8}$$

The estimate $\hat{\boldsymbol{\theta}}$ is a solution of (C8). The variance $\hat{\boldsymbol{\theta}}$ of $\boldsymbol{\theta}$ is obtained by linearizing (C8) for $\boldsymbol{\theta} \rightarrow \hat{\boldsymbol{\theta}}$:

$$\begin{aligned} &\text{var}\,\mathbf{p} = \left[\mathbf{J}^{\mathrm{T}}\mathbf{J}\right]^{-1}(\mathbf{J}\mathbf{y}) \\ &\mathbf{J} = [\mathbf{J}_1, \ldots, \mathbf{J}_n]^{\mathrm{T}} \qquad , \mathbf{y} = \left[\delta y_1^2, \ldots, \delta y_n^2\right] \\ &\mathbf{J}_i = \left[J_{i1}^2, \ldots, J_{ik}^2\right] \qquad , J_{ij} = \frac{\partial f(x_i|\boldsymbol{\theta})}{\partial p_j} \end{aligned} \tag{C9}$$

If $\mathbf{y}$ is ergodic and the measuring points are equally spaced, (C9) can be conveniently approximated with integrals:

$$\begin{aligned} &\text{var}\,\mathbf{p} = \Delta x(\delta y)^2\Psi^{-1}\Lambda \\ &\Psi = [\Psi_1, \ldots, \Psi_k]^{\mathrm{T}} \quad , \Psi_i = \left[\Psi_{i1}^2, \ldots, \Psi_{ik}^2\right] \quad , \Lambda = [\Psi_{11}, \ldots, \Psi_{kk}] \\ &\Psi_{ij} = \int_X \frac{\partial f(x|\boldsymbol{\theta})}{\partial p_i} \frac{\partial f(x|\boldsymbol{\theta})}{\partial p_j} \mathrm{d}x \end{aligned} \tag{C10}$$

A particularly simple case of (C10) is (9), where only one parameter is optimized ($\boldsymbol{\theta} = \theta$).

Notation

H	Magnetic field
M	Sample magnetization
m	Magnetization of a component
f	A general distribution function
θ	A general distribution parameter
$\hat{\theta}$	An estimate of θ
GG	Generalized Gauss distribution
SGG	Skewed Generalized Gauss distribution
μ_2	Mean value of a distribution
σ_2	Standard deviation of a distribution
s	Skewness of a distribution
k	Coefficient of excess kurtosis of a distribution
μ	Distribution parameter for the mean
σ	Distribution parameter for the standard deviation
q	Distribution parameter for the skewness
p	Distribution parameter for the kurtosis

[53] **Acknowledgments.** I would like to thank S. Spassov for testing CODICA and suggesting many useful improvements. I thank him and M. Fuller for providing me with some test samples. I am grateful to R. Enkin and M. Jackson for their constructive reviews and W. Lowrie for helping me with the writing task. This work was supported by the ETH research project 0-20556-00.

References

Bailey, M. E., and D. J. Dunlop, Alternating field characteristics of pseudo-single-domain (2–14 μm) and multidomain magnetite, *Earth Planet. Sci. Lett.*, *63*, 335–352, 1983.

Carter-Stiglitz, B., B. Moskowitz, and M. Jackson, Unmixing magnetic assemblages and the magnetic behaviour of bimodal mixtures, *J. Geophys. Res.*, *106*, 26,397–26,411, 2001.

Cisowski, S., Interacting vs. non-interacting single-domain behaviour in natural and synthetic samples, *Phys. Earth Planet. Inter.*, *26*, 56–62, 1981.

Cowan, G., *Statistical Data Analysis*, Oxford Univ. Press, New York, 1998.

Dunlop, D. J., The rock magnetism of fine particles, *Phys. Earth Planet. Inter.*, *26*, 1–26, 1981.

Dunlop, D. J., Coercive forces and coercivity spectra of submicron magnetites, *Earth Planet. Sci. Lett.*, *78*, 288–295, 1986.

Egli, R., and W. Lowrie, The anhysteretic remanent magnetization of fine magnetic particles, *J. Geophys. Res.*, *107*, 2209–2229, 2002.

Evans, M., N. Hastings, and B. Peacock, *Statistical Distributions*, John Wiley, New York, 2000.

Eyre, J. K., The application of high resolution IRM acquisition to the discrimination of remanence carriers in Chinese loess, *Stud. Geophys. Geod.*, *40*, 234–242, 1996.

Geiss, C. E., and S. K. Banerjee, A multi-parameter rock magnetic record of the last glacial–interglacial paleoclimate from south-central Illinois, USA, *Earth Planet. Sci. Lett.*, *152*, 203–216, 1997.

Halgedahl, S. L., Revisiting the Lowrie–Fuller test: Alternating field demagnetization characteristics of single-domain through multidomain glass-ceramic magnetite, *Earth Planet. Sci. Lett.*, *160*, 257–271, 1998.

Harrison, R. M., and J. Yin, Particulate matter in the atmosphere: Which particle properties are important for its effects on health?, *Sci. Total Environ.*, *249*, 85–101, 2000.

Hartstra, R. L., A comparative study of the ARM and Isr of some natural magnetites of MD and PSD grain size, *Geophys. J. R. Astron. Soc.*, *71*, 497–518, 1982.

Heslop, D., M. J. Dekkers, P. P. Kruiver, and I. H. M. van Oorschot, Analysis of isothermal remanent magnetization acquisition curves using the expectation-maximization algorithm, *Geophys. J. Int.*, *148*, 58–64, 2002.

Hüglin, C., Anteil des Strassenverkehrs an den PM10- und PM2.5-Immissionen, Bericht C4 des NFP 41, 2000.

Johnson, H. P., W. Lowrie, and D. Kent, Stability of anhysteretic remanent magnetization in fine and coarse magnetite and maghemite particles, *Geophys. J. R. Astron. Soc.*, *41*, 1–10, 1975.

Kruiver, P. P., M. J. Dekkers, and D. Heslop, Quantification of magnetic coercivity components by the analysis of acquisition curves of isothermal remanent magnetization, *Earth Planet. Sci. Lett.*, *189*, 269–276, 2001.

Lees, J. A., Mineral magnetic properties of mixtures of environmental and synthetic materials: Linear additivity and interaction effects, *Geophys. J. Int.*, *131*, 335–346, 1997.

Maher, B. A., and R. M. Taylor, Formation of ultrafine-grained magnetite in soils, *Nature*, *336*, 368–370, 1988.

Moskowitz, B. M., et al., Magnetic properties of magnetotactic bacteria, *J. Magn. Magn. Mater.*, *73*, 273–288, 1988.

Moskowitz, B. M., R. Frankel, and D. Bazylinski, Rock magnetic criteria for the detection of biogenic magnetite, *Earth Planet. Sci. Lett.*, *120*, 283–300, 1993.

Muxworthy, A. R., E. Schmidbauer, and N. Petersen, Magnetic properties and Mössbauer spectra of urban atmospheric particulate matter: A case study from Munich, Germany, *Geophys. J. Int.*, *150*, 558–570, 2002.

Robertson, D. J., and D. E. France, Discrimination of remanence-carrying minerals in mixtures, using isothermal remanent magnetisation acquisition curves, *Phys. Earth Planet. Inter.*, *82*, 223–234, 1994.

Shu, J., J. A. Dearing, A. P. Morse, L. Yu, and C. Li, Magnetic properties of daily sampled total suspended particulates in Shangai, *Environ. Sci. Technol.*, *34*, 2393–2400, 2001.

Stockhausen, H., Some new aspects for the modelling of isothermal remanent magnetization acquisition curves by cumulative log Gaussian functions, *Geophys. Res. Lett.*, *25*, 2217–2220, 1998.

Tarantola, A., *Inverse Problem Theory*, Elsevier Sci., New York, 1987.

Thompson, R., Modelling magnetization data using SIMPLEX, *Phys. Earth Planet. Inter.*, *42*, 113–127, 1986.

Verosub, K. L., and A. P. Roberts, Environmental magnetism: Past, present and future, *J. Geophys. Res.*, *100*, 2175–2192, 1995.

Wehrli, B., A. F. Lotter, T. Schaller, and M. Sturm, High-resolution varve studies in Baldeggersee (Switzerland): Project overview and limnological background data, *Aquat. Sci.*, *57*, 360–386, 1997.

Worm, H.-U., and M. Jackson, The superparamagnetism of Yucca Mountain Tuff, *J. Geophys. Res.*, *104*, 25,415–25,425, 1999.

Xu, S., and D. J. Dunlop, Toward a better understanding of the Lowrie–Fuller test, *J. Geophys. Res.*, *100*, 22,533–22,542, 1995.

Yu, L., and F. Oldfield, A multivariate mixing model for identifying sediment source from magnetic measurements, *Quat. Res.*, *32*, 168–181, 1989.

R. Egli, Institute of Geophysics, Eidgenossische Technische Hochschule, Zurich, CH-8093 Zurich, Switzerland. (egli@mag.iq.erdw.ethz.ch)